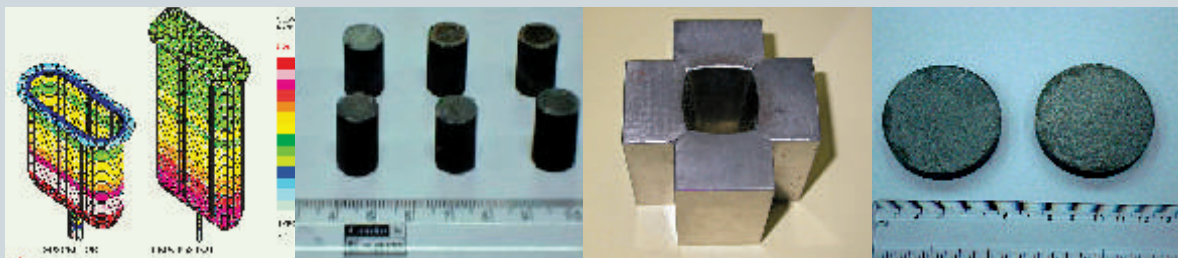




# BARC

## NEWSLETTER



### IN THIS ISSUE

- Thermal and Stress Analyses of Oblong Shaped Metallic Melter
- Analytical Performance of Refractometry in Quantitative Estimation of Isotopic Concentration of Heavy Water in Nuclear Reactor
- Characterization of High Level Liquid Waste Generated from Reprocessing of Power Reactor Spent Fuel
- Development of High Temperature Thermoelectric Materials and Fabrication of Devices
- Development and Fabrication of Superconducting hybrid Cable-In-Conduit-Conductor (CICC) for indigenous Fusion Programme
- Multi-Detector Environmental Radiation Monitor with Multichannel Data Communication for Indian Environmental Radiation Monitoring Network (IERMON)
- Mapping Interfaces in Magnetic Thin Films with Neutron Reflectometry

## In the Forthcoming Issue

1. **“Cyber-security, Personnel Tracking and Surveillance Solution”**  
D.K. Dixit et al.
2. **Friction Stir Welding of Al alloys**  
N.S. Kumbhar et al.
3. **Ground Response Analysis and Behavior of Single Pile in Liquefied Soils during Earthquake**  
V.S. Phanikanth et al.
4. **Precision-Micro-Nano Engineering**  
V.K. Suri et al.
5. **Radiation Processing of Temperate Fruits of Kashmir Valley**  
P.R. Hussain et al.
6. **Composite Polyamide Reverse Osmosis(RO) Membranes-Recent Developments and Future Directions**  
A.K. Ghosh et al.
7. **Matrix-assisted laser Desorption/Ionization Time-of-Flight Mass Spectrometry for Biomolecular Research**  
T. Jayasekharan and N.K. Sahoo

# Contents

## Research Articles

Thermal and Stress Analyses of Oblong Shaped Metallic Melter 1  
*S.M.Thorve et al.*

Analytical Performance of Refractometry in Quantitative Estimation of Isotopic Concentration of Heavy Water in Nuclear Reactor 7  
*K. Dhole et al.*

Characterization of High Level Liquid Waste Generated from Reprocessing of Power Reactor Spent Fuel 12  
*B.S.Tomar et al.*

## Technology Development Articles

Development of High Temperature Thermoelectric Materials and Fabrication of Devices 17  
*Deep Prakash et al.*

Development and Fabrication of Superconducting Hybrid Cable-In-Conduit-Conductor (CICC) for indigenous Fusion Programme 26  
*A.K. Singh et al.*

## Feature Articles

Multi-Detector Environmental Radiation Monitor with Multichannel Data Communication for Indian Environmental Radiation Monitoring Network (IERMON) 31  
*M.D. Patel et al.*

Mapping Interfaces in Magnetic Thin Films with Neutron Reflectometry 35  
*Saibal Basu and Surendra Singh*

## News & Events

- India and CERN: Visions for Future Collaboration 44
- Report on the Seminar "Nanotechnology and Its Applications" 45
- National Technology Day Celebration at BARC : a report 46

## BARC Scientists Honoured

## Editorial Committee

### Chairman

Dr. V. Venugopal,  
Director, RC&I Group

### Edited by

Dr. K. Bhanumurthy  
Head, SIRD

### Associate Editors for this issue

Dr. Madangopal Krishnan, MSD  
Dr. C. Srinivas, PsDD

### Members

Dr. V. Venugopal, RC&I Group  
Mr. C.S.R. Prasad, ChTD  
Dr. D.N. Badodkar, DRHR  
Dr. A.P. Tiwari, RCnD  
Dr. Madangopal Krishnan, MSD  
Dr. A.K. Tyagi, ChD  
Dr. P.V. Varde, RRSd  
Dr. S.M. Yusuf, SSPD  
Mr. Avaneesh Sharma, RED  
Dr. C. Srinivas, PsDD  
Dr. G. Rami Reddy, RSD  
Dr. S.K. Mukherjee, FCD  
Mr. G. Venugopala Rao, APPD  
Dr. A. Vinod Kumar, EAD  
Dr. Anand Ballal, MBD  
Dr. K. Bhanumurthy, SIRD  
Dr. S.C. Deokattey, SIRD

## *From the Editor's Desk ...*

The Founder's Day Special Issue of the BARC Newsletter will be released on the occasion of Founder's Day, in October 2011. As was done in the previous year, the issue will be printed only in the CD format. This year, we have hosted a web link on the homepage of BTS. DAE and other award winners are invited to login to the website and upload their papers directly. This would save a lot of time and effort and would help us in bringing out the Special Issue on time. Kindly note, that the last date for uploading all award winning papers for this issue, is 31<sup>st</sup> July, 2011.

This issue carries seven articles in various research categories and two important R&D contributions from BARC are of general interest. One is the work on an oblong shaped metallic melter, which would enhance the melter throughput for vitrification of high level waste. The other is the development and fabrication of Cable-In-Conduit-Conductor (CICC). This superconducting high-grade multifilamentary wire, would be used for our indigenous fusion programme.

Looking forward to contributions from all the award winners, on or before 31<sup>st</sup> July, 2011.



Dr. K. Bhanumurthy

On behalf of the Editorial Committee

# Thermal and Stress Analyses of Oblong Shaped Metallic Melter

S.M. Thorve, G. Sugilal and K.N.S. Nair  
Technology Development Division

## Abstract

Induction heated metallic melter with a circular cross section is presently employed in the Waste Immobilization Plant at Trombay for high level liquid waste vitrification. In order to enhance melter throughput, an oblong shaped metallic melter is being developed in the Nuclear Recycle Group. As part of the safety analysis, finite element based thermal and stress analyses of the oblong shaped metallic melter have been carried out. Based on the thermal analysis, it is recommended to directly heat the process vessel, to obtain higher glass pool temperature. Present study also shows that the top supported design results in a creep strain rate of 0.02 % per hour at the melter bottom, which restricts the melter life to 2000 hours. Therefore, a bottom supported design is recommended to reduce the creep strain rate and process pot deformation.

## Introduction

Induction heated metallic melter has been successfully employed in the Waste Immobilization Plant (WIP) at Trombay for high level liquid waste vitrification. A multi-zone induction heating system is used for heating an inconel susceptor, which surrounds the process pot. Thermal radiations from the susceptor in turn heat the inconel process pot in which the incoming waste stream and glass forming additives undergo boiling, drying, calcination and melting to form the vitrified product. At present, a process pot with circular cross section having a diameter of 300 mm is used in WIP Trombay. Although the present metallic melter has several advantages, its main limitation is the limited throughput. In order to enhance the melter capacity, an oblong shaped metallic melter is being developed in the Nuclear Recycle Group, based on the concept of elliptically-shaped metallic melter reported in literature.

As a part of the safety analysis, the thermal stresses and the deflections as well as sustained stresses in

the oblong shaped metallic melter were computed using finite element technique. This analysis was carried out in two parts: (i) thermal analysis to obtain temperature distribution in various components of melter and in glass pool, and (ii) stress analysis of both process pot and susceptor of the melter.

## Description of Oblong Shaped Metallic Melter

The metallic melter has two main vessels – a susceptor and a process pot. Fig. 1 shows the geometric details of melter vessels<sup>1</sup>. The susceptor is the outer vessel of the melter and made of 15 mm thick inconel 690 plates. Lower portion of the susceptor vessel is surrounded by electric induction coils. The process pot is an inner vessel of melter in which vitrification of high level waste takes place. It contains a glass pool during normal operation and has a drain pipe (freeze valve) at the bottom to drain out molten glass in to a canister. Process pot has 15 mm thickness and is made of

inconel 690. Both the susceptor and process pot are supported on respective flanges and free to expand downwards.

### Finite Element Analysis

Oblong shaped melter was analyzed using the finite element software NISA. Two types of three-dimensional solid elements - 8 noded hexahedron and 6 noded wedge elements were used for the analysis<sup>3</sup>. Finite element model of melter is made up of 55624 elements and 71914 nodes. Fig. 2 shows the finite element model of oblong shaped metallic melter.

### Thermal Analysis

Thermal analysis of melter was performed using finite element method to obtain accurate temperature distribution in melter components as well as molten glass pool<sup>2</sup>. All three modes of heat transfer were considered in the analysis and implemented by applying appropriate boundary conditions<sup>3</sup>. This analysis was carried out for the following three different cases:

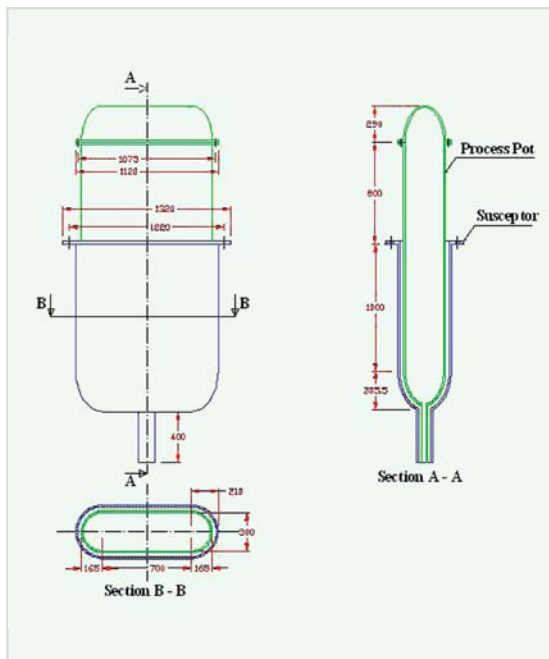


Fig. 1: Geometric details of oblong shaped metallic melter

### Case 1: Initial heating condition

In case 1, simulation of green heating of the empty melter was performed for verification of finite element model. During the green heating experiments, initial heating of the oblong shaped melter were carried out with empty process pot and temperature distributions across various parts of melter were measured employing thermocouples during this test.

### Case 2: Normal operation condition

In case 2, heat transfer analysis was completed for a normal operation condition, wherein a cold cap of low thermal conductivity is formed at the surface of glass pool. The liquid glass is assumed to be filled up to a height of 275 mm with a cold cap of 20 mm.

### Case 3: Soaking condition

In case 3, thermal analysis was done for soaking condition which corresponds to product homogenization. In this case, process pot contains a vitrified product ready for draining in to a canister.

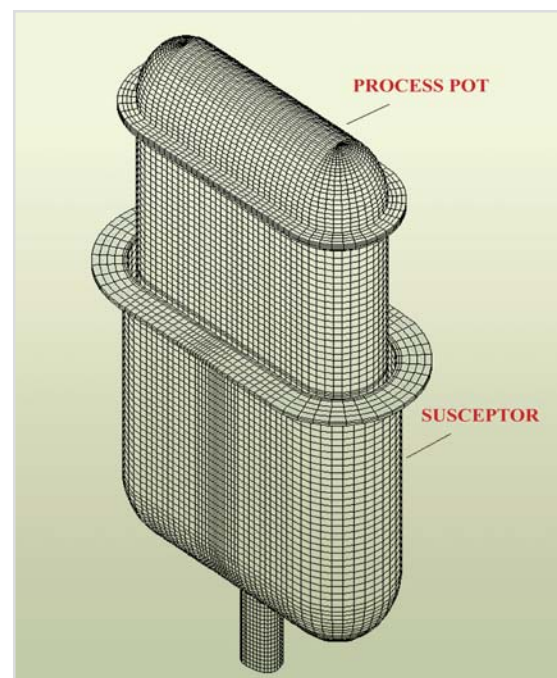


Fig. 2: Finite element model of oblong shaped metallic melter

### Stress Analysis

The objective of this analysis was to calculate the stress distribution pattern in the melter due to sustained loads (self weight, weight of glass, etc) and thermal loads. Susceptor and process pot are each supported at four locations on their respective flanges. Appropriate displacement boundary conditions were applied on the finite element model at support locations for this analysis<sup>4</sup>. For thermal stress analysis, nodal temperatures required as input boundary conditions were directly read from output result file of thermal analysis.

### Results

#### Results of Thermal Analysis

Temperature distributions in various parts of oblong shaped metallic melter were computed and maximum temperatures in melter vessels obtained for case 1 of the thermal analysis are summarized in Table 1. These results were used for model validation. Table 2 gives a comparison of experimental results and analysis results. The model predictions are in good agreement with experimental results and thereby, confirm the accuracy of finite element model and applied boundary conditions.

Table 1: Maximum temperatures for Case 1 of thermal analysis

Component	Maximum Temperature
Susceptor	1031 °C
Process Pot	876.2 °C

Table 2: Comparison of experimental and thermal analysis results

Maximum Temperature of Process Pot	
From Thermal analysis	From Experiment
876.2 °C	878 °C

An additional run for case 1 was carried out with increased power to induction coils surrounding the susceptor such that the susceptor temperature profile increased by about 100 °C. Maximum temperatures

obtained for different cases are compared in Table 3. Fig. 3 shows the temperature distribution in the melter components for revised case 1 with increased power level.

Table 3: Maximum temperatures for revised Case 1, Case 2 & Case 3 of thermal analyses

Component	Maximum Temperature		
	Revised Case 1	Case 2	Case 3
Susceptor	1131 °C	1131 °C	1131 °C
Process Pot	972 °C	866.5 °C	998.4 °C
Liquid glass	-	849.3 °C	991.3 °C

#### Results of Stress Analysis

The stresses in melter due to sustained loads (self weight and weight of glass) are summarized in Table 4. Fig. 4 shows the vonmises stress plots in susceptor and process pot.

Table 4: Stresses due to sustained loads

Component	Maximum Stress Intensity	Allowable Stress Intensity
Susceptor	1.94 N/mm <sup>2</sup>	43 N/mm <sup>2</sup>
Process Pot	2.0 N/mm <sup>2</sup>	43 N/mm <sup>2</sup>

Allowable stress intensity mentioned in Table 4 does not take into consideration damage due to creep phenomenon which will be quite significant at high temperatures. As the melter vessels experience high temperatures, creep strain rate and creep rupture life are important parameters which need to be evaluated<sup>5</sup>. These parameters were evaluated, based on the available creep curves at various temperatures. These results are shown for melter components in Table 5. The creep rupture life of process pot is the lowest and hence will govern

Table 5: Creep strain rate and creep rupture life of melter

Component	Creep Strain Rate	Creep Rupture Life
Susceptor	< 10 <sup>-5</sup> %/hr	> 10 <sup>5</sup> hours
Process Pot	0.02 %/hr	2000 hours

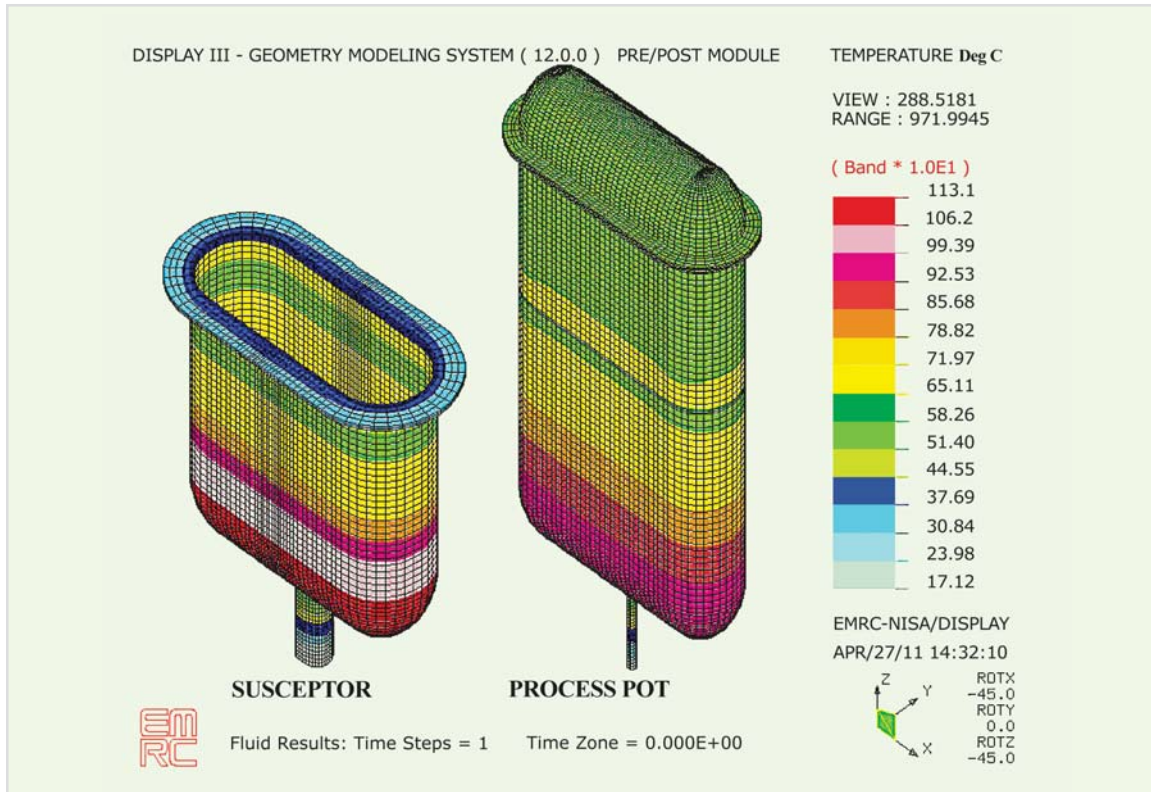


Fig. 3: Temperature distribution in melter for revised Case 1 of thermal analysis

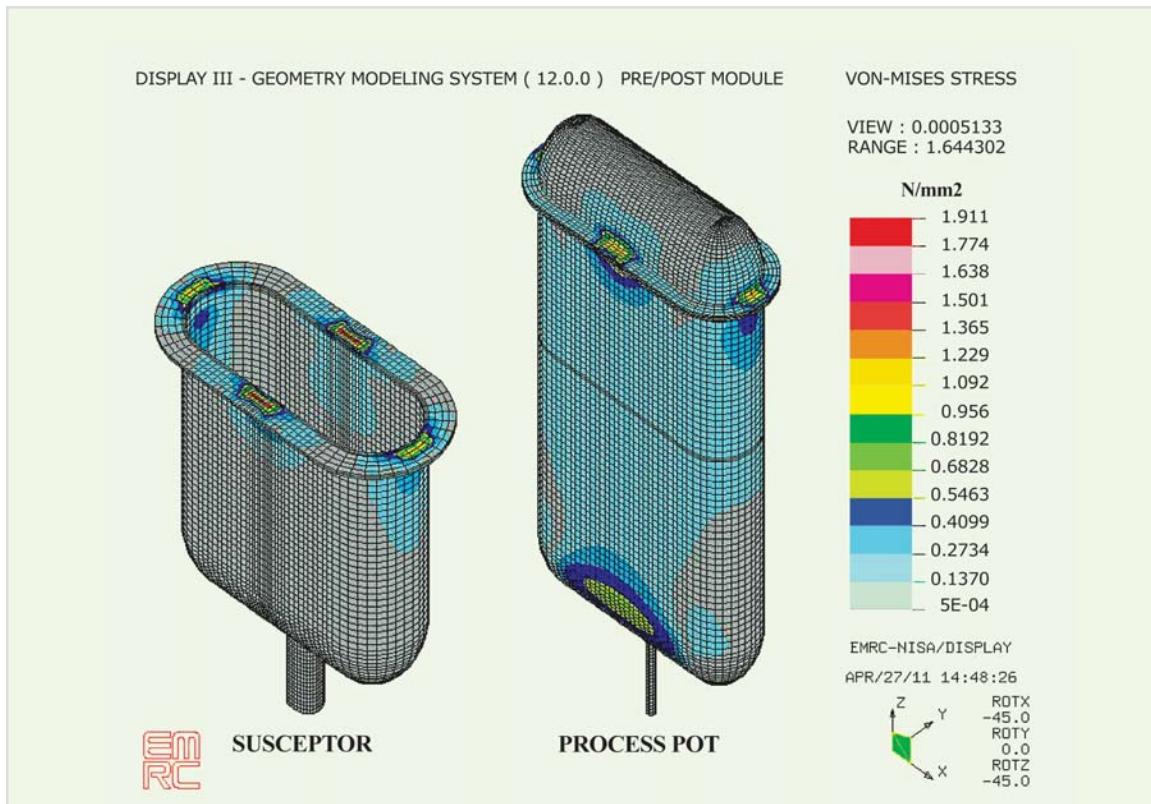


Fig. 4: Vonmises stress plot in susceptor due to sustained loads



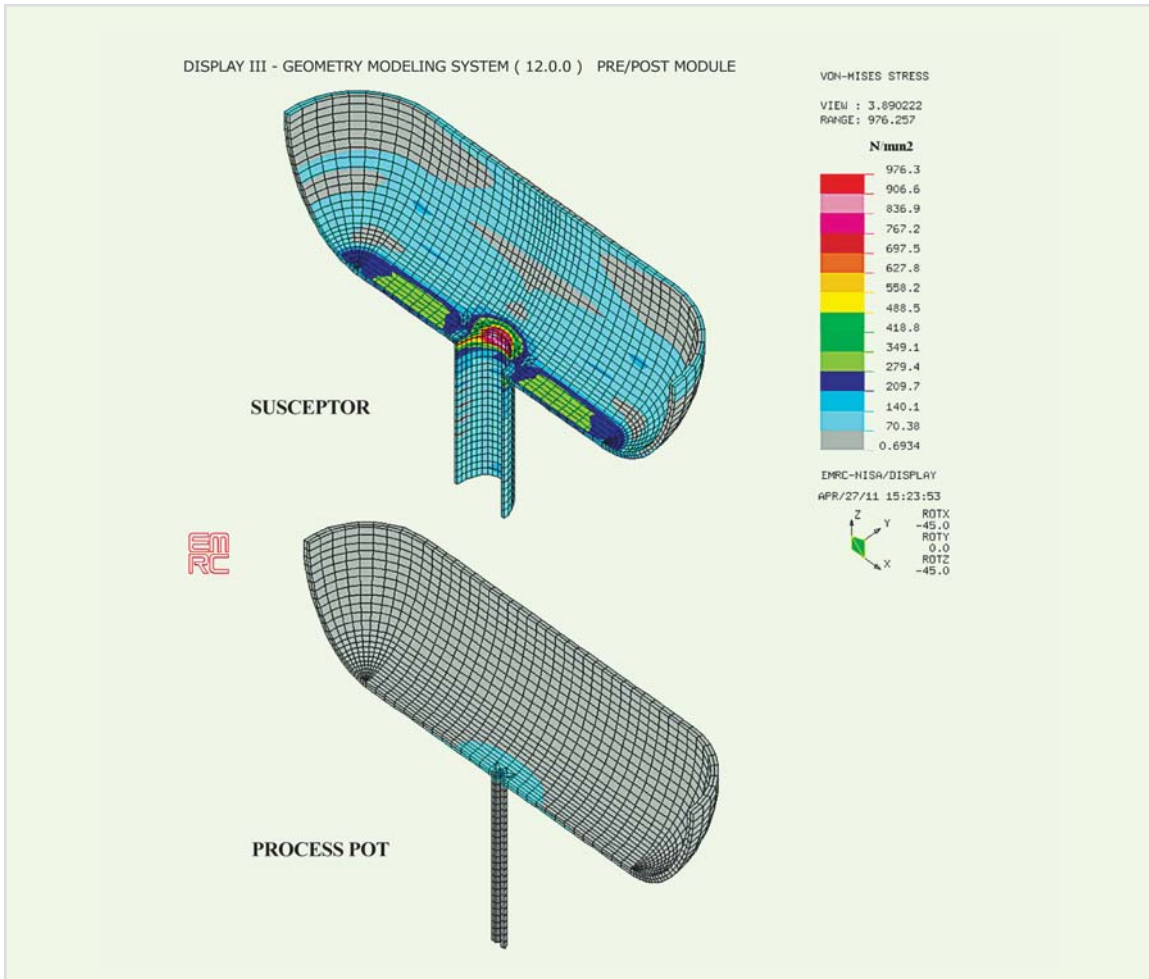


Fig. 5: Thermal stress plot in susceptor & process pot

melter rupture life. Thus the creep rupture life of melter is 2000 hours<sup>3</sup>.

Thermal stress analysis of melter was done for soaking condition as the maximum temperature in melter occurs during soaking condition (Case 3 of thermal analysis). Maximum thermal deflections and thermal stresses in melter thus obtained are summarized in Table 6. Fig. 5 shows the thermal stress plots in susceptor and process pots.

**Calculation of Fatigue Life**

Maximum thermal stress in susceptor occurs at the junction of vessel with bottom pipe. Similarly, maximum thermal stress in process pot occurs at the junction of vessel with drain pipe (freeze valve). These peak stresses are due to geometric discontinuity in these regions<sup>5</sup>. Thermal stresses are secondary in nature and will cause failure by fatigue after some cycles. The fatigue life calculated for

Table 6: Maximum thermal deflections and thermal stresses in melter

Component	Maximum thermal deflection		Maximum Thermal Stress
	Horizontal (at support bolts)	Vertical	
Susceptor	4.01 mm	20.54 mm	976.3 N/mm <sup>2</sup>
Process Pot	5.09 mm	28.31 mm	213.6 N/mm <sup>2</sup>

susceptor and process pot is 70 cycles and  $2 \times 10^6$  cycles respectively<sup>6</sup>.

### Conclusions

The results of thermal and stress analyses lead to the following conclusions:

- (i) Thermal analyses carried out shows that the susceptor temperature should exceed 1100 °C in order to obtain the glass pool temperature greater than 950 °C during soaking. Continuous exposure to temperatures greater than 1050 °C is undesirable for inconel 690. Therefore, it is recommended to design a melter without susceptor so that induction coils can directly heat the process pot. Thus, it will be possible to maintain maximum metal temperature under 1050 °C.
- (ii) Oblong bolt holes have been suggested on the flanges of susceptor and process pot instead of circular bolt holes in order to take care of horizontal thermal deflections at supporting locations.
- (iii) Fatigue life of melter has been calculated to be approximately 70 cycles. Creep rupture life has been calculated as 2000 hours.
- (iv) Present study shows that the top supported design results in a creep strain rate of 0.02 % per hour at the melter bottom, which restricts the melter life to 2000 hours. Therefore, a bottom supported design is recommended to reduce the creep strain rate and process pot deformation.

### References

1. R. K. Gupta, A. K. Singh, S. B. Patil, J. Jha, K. K. Haldar, S. D. Misra. "Engineering and manufacture of oblong shaped metallic melter for enhancing engineering throughputs". *ENC 2010 Transactions ISBN-978-92-95064-09-6, May 30 to June 02, 2010, Spain.*
2. F. P. Incropera & D. P. Dewitt. *Fundamentals of Heat and Mass Transfer. Wiley India Ltd., 2006*
3. Shailesh. M. Thorve, G. Sugilal, K. N. S. Nair. "Thermal and Stress Analysis of Oblong Shaped Melter". *BARC Internal Report, 2011.*
4. Engineering Mechanics Research Corporation. *User's Manual for NISA Display III and Heat III, 1998.*
5. J. F. Harvey. *Theory and Design of Pressure Vessels, CBS Publishers, 2001.*
6. ASME Boiler and Pressure Vessel Code, Section III, Div 1, Appendix 1, 2001.

# Analytical Performance of Refractometry in Quantitative Estimation of Isotopic Concentration of Heavy Water in Nuclear Reactor

K. Dhole, S. Ghosh, A. Datta, M. K. Tripathy and H. Bose  
Research Reactor Services Division

and

M. Roy and A. K. Tyagi  
Chemistry Division

## Abstract

The method of refractometry has been investigated for the quantitative estimation of isotopic concentration of D<sub>2</sub>O (heavy water) in a simulated water sample. Viability of Refractometry as an excellent analytical technique for rapid and non-invasive determination of D<sub>2</sub>O concentration in water samples has been demonstrated. Temperature of the samples was precisely controlled to eliminate effect of temperature fluctuation on refractive index measurement. Calibration performance by this technique exhibited reasonable analytical response over a wide range (1-100%) of D<sub>2</sub>O concentration.

*Keywords:* D<sub>2</sub>O; Heavy Water; Refractometry; Refractive Index; RI.

## Introduction

Heavy water (D<sub>2</sub>O) is used as a neutron moderator and coolant in Pressurised Heavy Water Reactors (PHWRs) and research reactors. The degradation of heavy water concentration in a reactor core results in loss of reactivity. Thus, a very accurate analysis of isotopic purity of heavy water in the core is necessary from reactivity point of view. Infrared absorption method is applied for this purpose because the method is very accurate and highly reproducible. However, infrared method has generally been applied to the isotopic analysis of heavy water with considerable success particularly at high and low D<sub>2</sub>O concentrations. Since the characteristic absorption bands are very intense, the concentration ranges analyzable by the use of respective bands through infrared technique are limited to narrow regions at either end of D<sub>2</sub>O concentration range. For analysis in the broad intermediate concentration range which includes

heavy water samples from intermediate stages of a production or upgradation facility, heavy water leakages from the different systems of PHWRs and research reactors, bed effluent of columns in the process of deuteration and inventory samples, the method of refractometry can be employed. Refractometric method may be used for rapid analysis of D<sub>2</sub>O [1-5] over the entire range from 1% to 100% D<sub>2</sub>O. Temperature of the sample and wavelength of light used are the most common experimentally controllable variables, that affect a refractive index (RI) measurement of liquid. For many liquids the index of refraction decreases by approximately 0.0005 for every 1°C increase in temperature. However, the variation for water is only about 0.0001/°C. In order to achieve a reasonable analytical reproducibility in the application of refractometry, a substantial importance has been given here to the control of temperature fluctuations.

In this study, weight percentage (wt.%) and mole percentage (mol%) concentration-variations, both have been used, to build a calibration model over the range of 1-100%.

## Experimental

### *Sample preparation*

A total of 13 samples were prepared for the measurements over the concentration range of 1 to 100 % D<sub>2</sub>O. The reference standard D<sub>2</sub>O of 99.96 wt.% ( ± 0.01 ) was obtained from Research Reactor Services Division, BARC, Trombay and appropriate amount of H<sub>2</sub>O was mixed with standard D<sub>2</sub>O in the preparation of samples. To minimize analytical error in sample preparation, all the samples were prepared in significant volume using 50ml conical flask. Ultra pure water (>18 MΩ cm<sup>-1</sup>, Milli-Q) was used throughout the whole experiment.

### *Measurement of Refractive Index and data processing*

RI measurements were done on a digital refractometer, RFM870 (Bellingham + Stanley Ltd., Longfield Road, Tunbridge Wells, Kent TN2 3EY, UK) equipped with artificial sapphire prism and Pt100 sensor (for monitoring sample temperature, Fig. 1).

Each RI measurement was done using the temperature control system by placing a small amount of liquid (~0.5 ml) onto the prism plate dish. All refractive index (<sup>20</sup>n<sub>D</sub>) values correspond to the D line of sodium (λ = 589.3 nm) at a particular temperature (20°C). Refractometer was conveniently calibrated with three standard liquids supplied by B+S Ltd., UK, such as BSDC & OILDC, BSLP & OILLP and AG refractometer calibration fluids with RI values (<sup>20</sup>n<sub>D</sub>) = 1.52256 ± 0.000074, (<sup>20</sup>n<sub>D</sub>) = 1.46990 ± 0.00074 and (<sup>20</sup>n<sub>D</sub>) = 1.33659 ± 0.000026 respectively. In order to build a calibration model

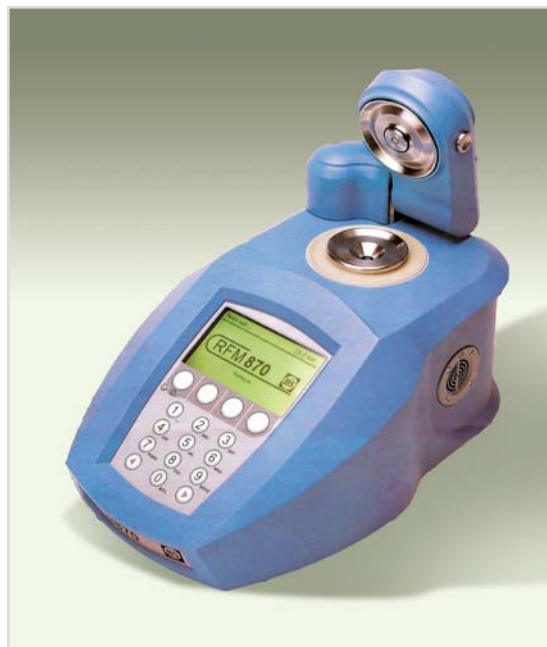


Fig.1: RFM870 Refractometer (Bellingham and Stanley Ltd., Longfield Road, Tunbridge Wells, Kent TN2 3EY, UK).

over the range of 1 % to 100 % D<sub>2</sub>O, concentrations in terms of wt.% and mol% both were considered. RI (<sup>20</sup>n<sub>D</sub>) data were imported into ORIGIN (Origin Lab Corporation, One Roundhouse Plaza, USA) along with data for wt.% and mol% concentration-variations before the calibration was performed. The experimentally determined RI (<sup>20</sup>n<sub>D</sub>) values for D<sub>2</sub>O-H<sub>2</sub>O mixtures at 20°C were then correlated to the polynomial form of refractive index equation. A total of 13 RI (<sup>20</sup>n<sub>D</sub>) measurements from 13 samples were divided into 7 RI data for calibration and 6 RI data for the prediction set serving as a validation set.

## Results and Discussion

### *Features for refractometric measurement*

The refractive index of liquids changes significantly with temperature. It is important that the temperature of a sample is to be constant throughout its mass before an accurate reading can be taken. The

sapphire prism together with the sample dish and lid over it can help for achieving optimal thermal conductivity and low-volume containment of the sample which enables rapid thermal equilibration with the prism surface and subsequent temperature stability of the sample for the duration of the reading. A highly stable optical system coupled with a thermally self-regulating detection system, with enhanced resolution, provides accurate reading in the shortest possible time. An intelligent electronic control system coupled with a twin-probe sensor, which accurately pinpoints the prism surface temperature, enables the system to achieve and maintain the sample at the prescribed temperature. A powerful system of Peltier devices and thermal insulation ensures rapid attainment of sample target temperature. A separate multiple probe system continuously monitors the internal environment of the instrument and actively compensates any thermal fluctuations to optical and detector components.

Table 1: Performance of Refractometer

Model RFM870	Refractive Index
Range minimum	1.30
Range maximum	1.70
Display resolution	0.00001
Repeatability	± 0.00002
Temperature stability	± 0.05 °C

Performance of the instrument is described in Table 1.

**Quantitative calibration**

Fig. 2 shows the behavior of the refractive index property of the samples prepared with various concentrations in terms of wt.%.

Interestingly, the experimentally determined RI ( $^{20}\eta_D$ ) values for D<sub>2</sub>O-H<sub>2</sub>O mixtures at 20°C do follow polynomial relation of higher order with wt.% variation, instead of linear relation. As observed from

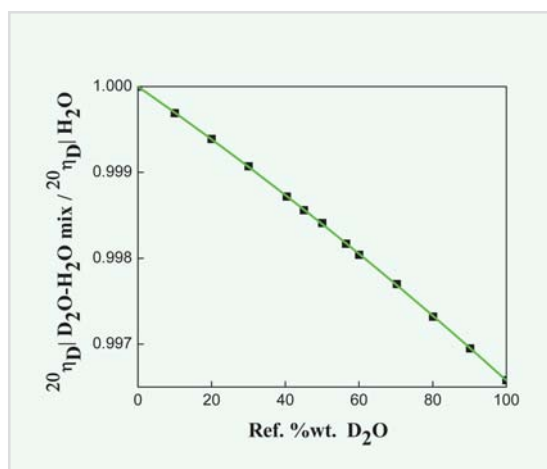


Fig. 2: Behavior of Refractive index for wt% variation.

experimental results, data could be correlated to the following form  $^{20}\eta_D$  (D<sub>2</sub>O-H<sub>2</sub>O mix) /  $^{20}\eta_D$  (H<sub>2</sub>O) =  $a_0 + a_1x + a_2x^2$  where  $x$  is the weight percentage of D<sub>2</sub>O in D<sub>2</sub>O-H<sub>2</sub>O mixture. This equation is very much useful particularly in the quantitative estimation of wt.% of D<sub>2</sub>O where the values of coefficients  $a_0$ ,  $a_1$  and  $a_2$  are computed as  $1.0 \pm 6.17592 \times 10^{-6}$ ,  $-2.98051 \times 10^{-5} \pm 2.67782 \times 10^{-7}$  and  $-4.42277 \times 10^{-8} \pm 2.56381 \times 10^{-9}$  respectively. However, for analytical purpose, we need to know the potential of each of the calibration method. Therefore, both wt.% and mol% concentration-variations are used in the calibration model for their assessment purpose. First, wt.% variation was used to build a quantitative calibration model. The refractive index was used to correlate with the concentration of D<sub>2</sub>O by linear regression method. The resulting calibration equation was  $y$  (RI:  $^{20}\eta_D$ ) =  $-4.5695 \times 10^{-5} \times x$  (wt.%) + 1.33309 with the correlation coefficient ( $R^2$ ) of 0.99826. Then the resulting standard error of calibration (SEC) was calculated. Using the refractive index data in the

Table 2: Calibration results using wt% and mol%

Calibration method	SEC	SEP
wt. %	1.32	0.98
mol%	0.31	0.25

prediction set, the standard error of prediction (SEP) was also calculated. The results are summarized in Table 2.

The achieved SEC and SEP were 1.32 and 0.98 wt.%, respectively. In Fig. 3(a), filled and open circles represent the calibration and prediction data, respectively. As shown in this figure, when wt.% was used, a fairly good correlation was achieved between the reference and the predicted concentrations. In order to ensure the calibration performance, mol%- variation method has also been accounted. Hence, the cross-validation was performed, in the same way as considered in wt.%-variation method, by dividing the data set into two segments to assign 54% of data into calibration, and the other 46% of data for validation.

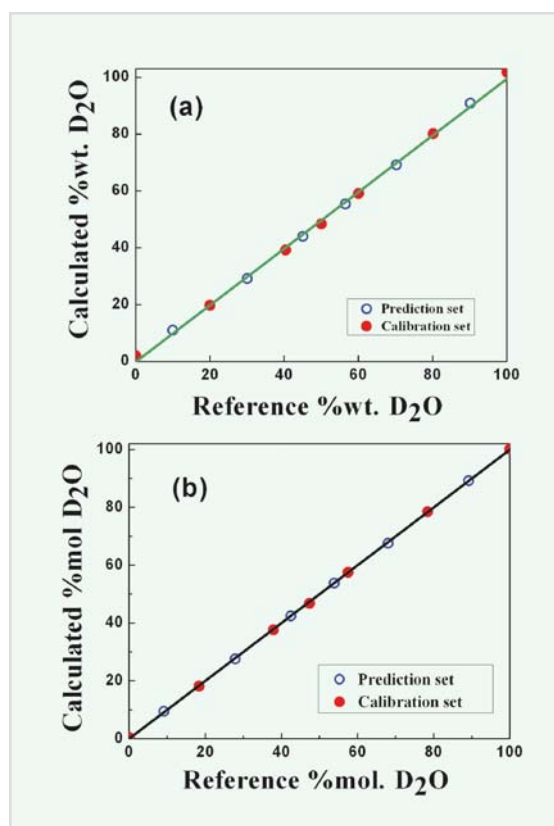


Fig. 3: Concentration correlation plot using (a) wt.% and (b) mol% variations. Filled and open circles represent the calibration and prediction data respectively

The resulting calibration equation was  $y$  ( $RI: {}^{20}\eta_D$ ) =  $-4.57319 \times 10^{-5} \times x$  (mol %) + 1.33302 with the correlation coefficient ( $R^2$ ) of 0.9999. The plot in Fig. 3 (b) shows the correlation between reference concentrations and RI measurements. Here also, filled and open circles represent the calibration and prediction data, respectively. The calibration and prediction data correlate very well with the reference data. The resulting SEC and SEP are summarized in Table 2.

The concentrations of D<sub>2</sub>O in the prediction data set were predicted with a SEP of 0.25 obtained in mol%-variation method. The resulting SEP is considerably improved compared to 0.98 obtained in wt%-variation method. Both SEC and SEP are significantly improved when mol%-variation method has been employed. The achieved SEP is acceptable from the viewpoint of rapid isotopic analysis of D<sub>2</sub>O concentration in Nuclear Reactor.

## Conclusion

The method of Refractometry for the analysis of D<sub>2</sub>O has been studied, to monitor the concentration over the entire range from 1 % to 100 % D<sub>2</sub>O. The method is extremely important for an alternative quantitative analysis because of its simplicity and very small volume of sample requirement. The measurement of refractive index property with the application of temperature control has been utilized here, for the purpose of the quantitative estimation of isotopic concentration of D<sub>2</sub>O in nuclear reactor. The present study indicates that the polynomial form of refractive index equation for wt.% variation method and the calibration model based on linear regression analysis for mol% variation method are the most suitable ways to predict D<sub>2</sub>O concentration accurately in the application of refractometry.

However, there are several issues yet to be addressed. The prime issue is the difficulty for isotopic analysis

of D<sub>2</sub>O through this method, with increase in impurity content (cationic/anionic) and turbidity in the accumulations of heavy water from different locations at the site during reactor operation. Here, standard D<sub>2</sub>O and ultra pure H<sub>2</sub>O were used throughout this study in the preparation of samples i.e. conductivity of the samples prepared is kept very low. This is directly related with the refractive index of a medium because of the accompanying change in density. Therefore, the behaviour of index of refraction for heavy water samples containing dissolved solids, oil, organic matters etc. needs to be explored.

### Acknowledgement

The authors are thankful to Mr. R. C. Sharma, Head RRSD, BARC for his keen interest and constant encouragement in the work.

### References

1. G. P. Baxter, L. L. Burgess and H. W. Daudt, *J. Am. Chem. Soc.*, 33 (6), 893 (1911).
2. E. Ingelstam, E. Djurle and L. Johansson; *J. Opt. Soc. Am.* 44, 472 (1954).
3. J.E. Bertie, M.K. Ahmed and H.H. Eysel; *J. Phys. Chem.* 93, 2210 (1989).
4. N.N. Kalnin, I.A. Baikalov and S.Yu. Venyaminov; *Biopolymers* 30, 1273 (1990).
5. R.P. Shukla and D.V. Udupa; *Optics & laser technology* 32, 355 (2000).

# Characterization of High Level Liquid Waste Generated from Reprocessing of Power Reactor Spent Fuel

**B.S.Tomar**

Radioanalytical Chemistry Division

*and*

**M.S. Murali and S.V. Godbole**

Radiochemistry Division

*and*

**K. Radhakrishnan**

Fuel Reprocessing Division

*and*

**P.B. Gurba**

PREFRE, Tarapur

## Abstract

High level Liquid Waste (HLW) is generated during the reprocessing of spent nuclear fuel which is used to recover uranium and plutonium. More than 99% of the radioactivity generated during the burning of nuclear fuel in the reactor is present in HLW. For the efficient management of HLW either by vitrification in the suitable borosilicate glass matrix, or partitioning and transmutation (P&T) of the minor actinides and long lived fission products, it is desired to assay the HLW for its constituent stable elements as well as radioactive content. The present article gives a brief account of an exercise carried out recently to characterize the HLW from PREFRE, Tarapur.

## Introduction

Reprocessing of the spent nuclear fuel is an integral part of the Indian Atomic Energy programme, as the Pu produced during the first stage of power generation through PHWRs, can be separated and utilized in the second stage, that is, in fast breeder reactors. However, the reprocessing of the spent nuclear fuel results in the generation of large volumes of wastes. The high level waste (HLW) contains more than 99% of the total radioactivity generated during the burning of the fuel in the reactor and requires utmost consideration owing to the presence of long-lived radionuclides, which constitute minor actinides, (Np, Am, Cm) along with traces of U and Pu, and the long-lived fission products, viz.,  $^{90}\text{Sr}$ ,  $^{93}\text{Zr}$ ,  $^{99}\text{Tc}$ ,  $^{129}\text{I}$ ,  $^{135,137}\text{Cs}$ ,  $^{154,155}\text{Eu}$ ,

etc. The HLW is at present vitrified in borosilicate glass matrix which is being stored in Solid Storage Surveillance Facility (SSSF), to allow for the decay of the short-lived radionuclides and for observing the vitrified waste product. Eventually, the waste form will be buried in a Deep Geological Repository (DGR) so as to keep it away from the public domain for millions of years. Fig.1 gives the activity of long lived radionuclides, present in HLW as a function of time.

Another strategy, which is gaining ground towards reducing the radiotoxicity of the HLW is transmutation of the long-lived minor actinides and fission products in incinerators based on the Accelerator Driven Subcritical (ADS) reactor system,



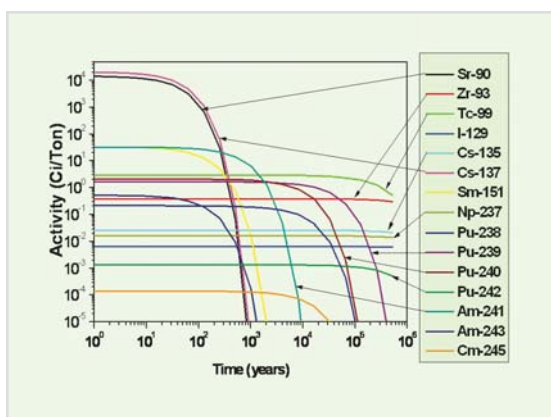


Fig. 1: Profile of activity of long lived radionuclides present in HLW per ton of spent PHWR fuel (6700 MWD/t). Assuming 99% of Pu is removed.

wherein the high energy proton accelerator ( $E_p = \sim \text{GeV}$ ) having several milli-amperes of beam current is used, to cause spallation reaction in a suitable heavy target (Pb, Bi, Ta, W) and the spallation neutrons are used, to induce fission/transmutation in the fuel elements made of minor actinides (MAs)/ fission products (FPs). Characterization of the HLW is important for actinide partitioning as the inventory of MAs in the HLW has not been evaluated accurately in the past. A brief account of the work carried out towards the characterization of the HLW is given below.

### Inter-laboratory comparison exercise for the determination of elemental composition of Simulated High Level Waste (SHLW)

With an aim to bring in uniformity in the methodology for determination of elemental composition of HLW by different laboratories, an Inter-Laboratory Comparison Exercise (ILCE) was carried out with the simulated HLW of different types of reactors, namely, Research Reactor (RR), PHWR power reactor (PHWR) and Fast Breeder reactor (FBR). The SHLW corresponding to RR (burn up = 1000 MWD/t) and PHWR (burn up = 6700 MWD/t) were prepared at the Waste Management Division, BARC, while that for FBR (burn up = 150,000 MWD/t) was prepared at the Chemistry

Group, IGCAR. Trace metal concentrations in the SHLW were determined by Inductively Coupled Plasma – Atomic Emission Spectrometry (ICP-AES), after separation of uranium, wherever present. All the laboratories followed the same procedure.

In the case of elements present in concentrations more than 10 mg/L of SHLW, the results from different laboratories were in agreement within 15%, while in case of elements present at lower concentrations than 10 mg/L, the data was in agreement within 50%. This extent of agreement is considered to be fairly acceptable. In some cases the deviations were more, which was attributed to the standard solution used for calibration of the instrument. After taking the new standard, the data was found to be in agreement with the other laboratories. Thus the ILCE helped in ascertaining the uniformity of the methodology as well as the standards used for determination of elemental concentrations in the HLW.

### Characterization of HLW from PHWR

The gamma radiation dose given by the HLW is extremely high ( $> 1 \text{ R/hr per ml}$ ) and hence can not be handled in ICP-AES instruments even after dilution by a factor of 50, which is the desired level of dilution. In the case of short cooled HLW, the gamma dose is mainly due to  $^{137}\text{Cs}$ ,  $^{106}\text{Ru}$ ,  $^{144}\text{Ce}$ ,  $^{134}\text{Cs}$  along with Bremsstrahlung from  $^{90}\text{Sr}$ . In the case of long cooled HLW, the dose is mainly to  $^{137}\text{Cs}$  and Bremsstrahlung from  $^{90}\text{Sr}$ . Therefore, experiments were carried out to separate  $^{137}\text{Cs}$  from HLW.

### Separation of Cesium from HLW

The HLW from the process stream of PREFRE plant was contacted with an organic phase consisting of chlorinated cobalt dicarbolyde (CCD) dissolved in 20% nitrobenzene and 80% xylene under constant stirring to separate cesium. The dose in the aqueous fraction was found to decrease by a factor of 3,

compared to the original solution. More than 99% of  $^{137}\text{Cs}$  was separated by the solvent extraction with CCD in three contacts. The high gamma dose in the HLW raffinate was found to be due to  $^{106}\text{Ru}$ ,  $^{144}\text{Ce}$ ,  $^{154}\text{Eu}$ ,  $^{125}\text{Sb}$ , etc. Apart from the Cs-separated HLW, 0.2 ml of HLW, in duplicate, was sampled directly for the analysis of elemental composition, alpha, beta and gamma activity.

### ***ILCE for determination of elemental concentrations in the HLW from PREFRE***

1 ml from the stock solutions of HLW from which Cs had been separated (HLW-CCD) and direct HLW were supplied to different laboratories, namely, PREFRE, RCD and FRD for determination of elemental concentration as well as radiometric assay. Samples were also supplied to WIP, Tarapur for radiometric assay. Table 1 gives the average concentrations of the various elements in the HLW.

Comparison of the measured concentrations with the theoretically computed concentrations shows that, for all fission products, except Pd, the ratio of the measured value to calculated values is close to 4, which can be explained in terms of the dilution factor (800 L/t for computed concentrations and 3000 L/t for actual HLW). In the case of Pd the ratio is very high indicating the loss of Pd during dissolution of spent fuel. Zr concentration in HLW was very small, which could be due to its distribution in the PUREX streams and hence are not reported.

### ***Radiometric assay of HLW***

For radiometric assay, the HLW was diluted to bring down the activity level sufficiently low to reduce the dead time of the detection system. Estimation of gross alpha and beta activity in HLW was carried out by alpha beta discriminating liquid scintillation counter. A typical 2-D spectrum is shown in Fig. 2.

The gross alpha and beta activities were calculated after applying dilution factors. The values were found to be in good agreement with those obtained by alpha spectrometry. For gamma counting, triplicate

Table 1: ILCE on HLW from PREFRE: (A) ICP-AES. (All concentrations are in mg/L. Dilution factor =3000L/ton of uranium.)

Element	Average Conc. (ppm)	%RSD	Ratio. Theory/ Expt
Sr	54.3	5.9	3.86
Y	27.6	9.9	4.16
Mo	243	9.2	3.52
Ru	158	3.1	3.42
Rh	41	37.9	3.65
Pd	12.7	35.4	25.9
Ba	96	22.2	3.95
La	91	13.1	3.39
Ce	168	21.1	3.65
Pr	68	25	4.13
Nd	278	10.9	3.69
Sm	60	3.2	3.56
Cr	182	19.7	-
Fe	743	15.3	-
Mn	21.5	16.3	-
Na	822	10.3	-
Ni	100	16.6	-

Average value of  $R(\text{computed/measured}) = 3.73 \pm 0.27$

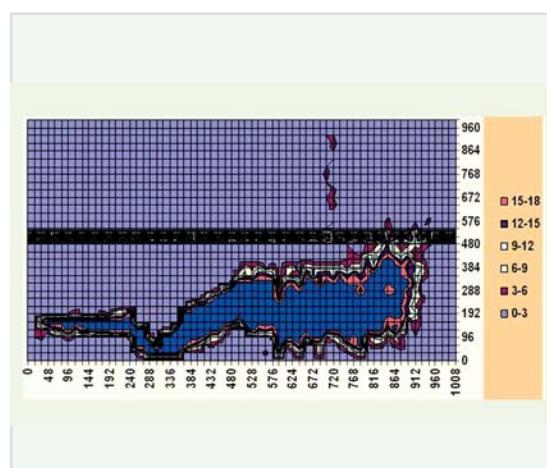


Fig. 2: 2D spectrum of HLW in alpha beta discriminating liquid scintillation counter.

samples were made from direct and CCD separated HLW. The samples were made in the form of 5 ml liquid samples in 20 ml capacity glass counting vials and counted on a HPGe detector coupled to 4k channel analyzer. The dead time of the counting was kept below 10% and the spectra were acquired in live time mode. Typical gamma ray spectra of the direct HLW and Cs separated HLW are shown in Fig.3.

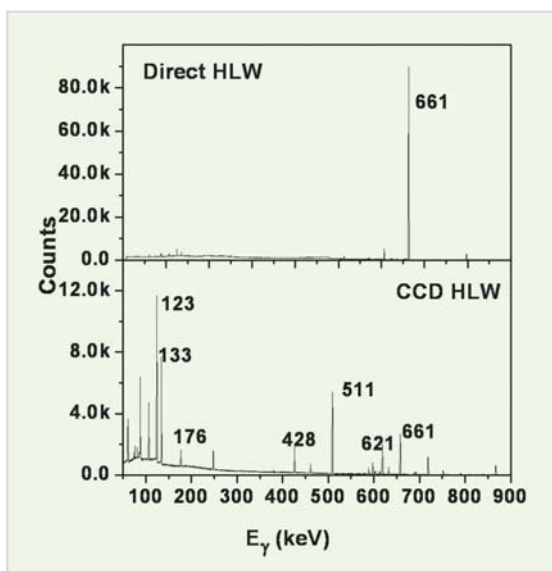


Fig. 3: Gamma spectra of HLW (direct and Cs separated)

The 661 keV peak of <sup>137</sup>Cs which dominated the gamma spectrum of the direct HLW, is smaller than many of the other radioisotopes after the separation. More than 99.9 % of <sup>137</sup>Cs was found to be separated by CCD. The activity of the radionuclide was obtained from the peak area using the known gamma ray abundance and, detection efficiency. Table 2 gives the results of gross alpha, beta counting and radionuclidic assay by HPGe. Measurements were carried out at four laboratories, namely, RCD, PREFRE, WIP and FRD. The standard deviation of the data from the four laboratories is less than 20%.

**Minor actinide assay in HLW**

Preliminary investigation of appropriately diluted samples by alpha spectrometry revealed well resolved

Table 2: Results of radiometric assay of HLW

Radionuclide	Average activity (iCi/L)	St. dev.
Gross alpha	99.8	13.8
gross beta	21009.9	2919.7
Cs-137	6932.4	1098.05
Cs-134	268	31.6
Ru-106	318.7	81.2
Ce-144	245.4	60.4
Sb-125	71.95	17.9
Eu-154	109.7	17.5
Eu-155	70.2	—
Am-241	53.1	—
Sr-90	4660	288.4

peaks of <sup>241</sup>Am, <sup>244</sup>Cm and <sup>242</sup>Cm (Fig.4a) and hence they were estimated directly. The peaks due to Pu and Np were not well resolved. It was, therefore, decided to estimate Np and Pu after their separation from Am and Cm. Np and Pu, were oxidized to VI state by ~5 mg of solid AgO in ~0.5M nitric acid and separated from HLW by solvent extraction into

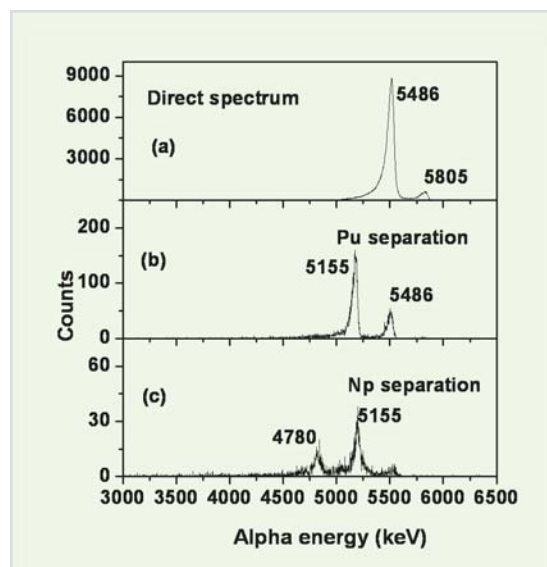


Fig. 4: Alpha spectra of HLW, before and after separation of Pu and Np

15% TRPO + 10% TBP in dodecane. The peak due to  $^{239,240}\text{Pu}$  was resolved (Fig.4b), however, that due to  $^{237}\text{Np}$  could not be resolved, owing to its low activity and degraded alpha spectrum. For the estimation of Np, 0.2 M ferrous sulphamate and a pinch of hydroxylamine hydrochloride were added to keep Np in IV and Pu in III state, followed by extraction of Np(IV) into 0.5 M HTTA in xylene.  $^{239}\text{Np}$  was used as a tracer for determination of chemical yield. The resulting alpha spectrum is shown in Fig.4c.

### Conclusion

ILCE for elemental composition of SHLW by ICP-AES showed good agreement among the different laboratories as well as with the actual values. By separation of  $^{137}\text{Cs}$ , the gamma dose of HLW could be brought down to workable levels. ILCE of HLW by ICP-AES showed reasonably good agreement among the results from different labs as well as the calculated values. In the case of ILCE for gamma spectrometry the agreement was fairly good. Minor actinide assay in HLW was carried out successfully to obtain their concentrations. The sum of the MA alpha activity agrees with the gross alpha from all the labs.

### Acknowledgement

Authors thank all the members of the Task force on characterization of high level waste for their valuable contributions and suggestions. Special thanks are due to Dr. Baldev Raj, Director, IGCAR, Dr. V.Venugopal, Director RC&I Group, BARC, Dr. P.R.Vasudev Rao, Director Chemistry Group, IGCAR, Dr. V.K.Manchanda, Head, RCD, BARC, Mr. R.D.Changrani, Chief Superintendent NRG Projects, Tarapur, Mr. Kanwar Raj, Head, WMD, and Mr. P.K.Dey, Head, FRD for their guidance and support during the execution of this task. We acknowledge the contribution of participating laboratories namely, RCD, FRD, WMD, PREFRE, CG, IGCAR, KARP, BARC facilities, in the ILCE of SHLW. The efforts of Dr. P.G.Kulkarni, Mr. K.K.Gupta, Mr. D.K.Pant, Dr. (Mrs.) T.P.Valsala, Mr. P.K.Mishra, Dr. T.K.Seshgiri, Dr. S.K.Thulasidas, during analysis of actual HLW from PREFRE, Tarapur are gratefully acknowledged. Thanks are due to Dr. P.V.Achutan for theoretical calculations of the concentration of fission and activation products in the HLW.

# Development of High Temperature Thermoelectric Materials and Fabrication of Devices

Deep Prakash, R.D. Purohit, M. Syambabu and P.K. Sinha

Energy Conversion Materials Section

and

R.Tewari

Materials Science Division

## Abstract

Thermo Electric Conversion (TEC) is a technique, where heat is directly converted into electrical energy. Development of thermoelectric materials which operate at temperatures up to 700–900°C may be an attractive proposition, due to its potential application to the proposed high temperature nuclear reactors. Technologically important high temperature thermoelectric materials and their prototype devices have been developed in the Energy Conversion Materials Section of the Materials Group. Two types of materials i.e. FeSi<sub>2</sub> based intermetallic and mixed oxide ceramic materials have been synthesized and characterized, for high temperature thermoelectric properties, and then they were consolidated and finally integrated into miniature devices. A two-couple miniature device consisting of pins of dimensions 4 x 4 x 20mm, made up of *n*-type Fe<sub>0.94</sub>Co<sub>0.06</sub>Si<sub>2</sub> and *p*-type Fe<sub>0.91</sub>Mn<sub>0.09</sub>Si<sub>2</sub> intermetallics, exhibited 8μW power output at 100 °C which increased to 3 mW at 600 °C hot end temperature. On the other hand, a two-couple device made up of oxide ceramic materials, namely, *n*-type Ca<sub>0.92</sub>La<sub>0.08</sub>MnO<sub>3</sub>, as well as *p*-type Ca<sub>2.75</sub>Gd<sub>0.25</sub>Co<sub>4</sub>O<sub>9</sub> showed power out put of 18 mW at a hot end temperature of 750 °C.

## Introduction

Thermo Electric Conversion (TEC) is based on the direct transformation of heat into electrical energy [1]. As a consequence, this mode of power generation eliminates conventional steam cycle, and its related complexities. On the other hand, total amount of energy which can be made available is only a fraction of Carnot efficiency, thus thermoelectric conversion generally has lower efficiencies (up to 10%). Nonetheless, TEC is one of the most attractive techniques for futuristic electricity production due to some unique benefits it offers. Since the TEC devices do not involve any moving parts, they are silent and may require little or no maintenance. Further, the working of the device does not depend on the source of heat.

Therefore, heat source could be from heat produced by burning of fuel gases to radioactive decay heat.

Historically, TEC was first employed for providing electric power to spacecrafts. However, terrestrial applications are equally attractive, particularly for the utilization of spent heat, and for unmanned operations at remote locations [2]. The technology development of thermoelectric conversion has been limited so far to a few developed countries viz. USA, Japan, Canada, Germany etc. Majority of the thermoelectric converters developed are based on materials like Bi-Te and Pb-Te etc. which limit their operations to below 400°C. In the context of new and renewable energy technologies for hydrogen energy, fuel cells, high temperature nuclear reactors etc., it becomes imperative to develop materials and

devices which can operate at higher temperatures, in order to utilize high grade waste heat. However, development of TEC for higher temperature applications involves a number of material related issues. These include oxidation resistance at higher temperatures, phase transformations or decompositions to non-thermoelectric phases and strong temperature dependence on thermopower. In addition, technologically, the development of high temperature contacts with good electrical, thermal and mechanical properties is one of the impeding steps in realizing the TEC technology.

The intermetallic  $\beta$ -FeSi<sub>2</sub> phase, Si-Ge alloy and some oxides such as Ca<sub>3</sub>Co<sub>4</sub>O<sub>9</sub>, BaPbO<sub>3</sub>, and CaMnO<sub>3</sub> are potential candidate materials for high temperature thermoelectric applications, due to their high stability and good figure of merit (Z). Though few laboratory scale miniature demonstration devices based on  $\beta$ -FeSi<sub>2</sub> have been demonstrated [3-5], commercial exploitation is yet to be achieved. Similarly, development of oxide TE devices is also in a state of infancy [6-8]. On the other hand, systems based on Si-Ge have been used for specific applications like spacecrafts [9]. They have so far not come to commercial domain.

This article describes the synthesis and characterization of high temperature thermo-electric materials, and the fabrication of miniature devices carried out at ECMS, BARC.

### Thermoelectric power generation

Thermoelectric power generation is primarily based on Seebeck effect, which refers to the development of a voltage ( $\Delta V$ ) in a conductor, when it is placed in a temperature gradient ( $\Delta T$ ). The proportionality constant S is termed as Seebeck constant. Thus,

$$S = \Delta V / \Delta T$$

The voltage will be positive or negative depending on whether majority carriers in the materials are positive, like holes, or negative such as electrons. Based on this definition, the materials are termed as

n-type or p-type. Connecting the n-type and p-type thermo-elements in a configuration of electrically in series, but thermally in parallel, as shown in Fig. 1, results in the summation of generated voltage. A thermoelectric device termed as power module joins many such 'legs' for large voltage output. Merely possessing high value of S does not merit its choice for use in power generation. The criterion for a suitable material depends on its 'Figure of merit' Z, which is defined as:

$$Z = S^2 / (\kappa r)$$

where, S is Seebeck coefficient,  $\kappa$  is thermal conductivity and r is electrical resistivity of the material. The product ZT (where T is operating temperature) is known as dimensionless figure of merit. The figure of merit directly relates to efficiency which is shown in Fig. 2. Therefore, maximizing the value of ZT has been one of the most important goals of materials scientists and engineers. Though there is no theoretical limit on the value of ZT, till date, the maximum value reported is around 2. Since ZT also is a strong function of temperature (Fig.3), its peak value generally determines the application temperature. In order to 'flatten' the temperature dependence of the devices, layered composite materials as well as Functionally Gradient Materials (FGM) have been envisaged. Further, the heat

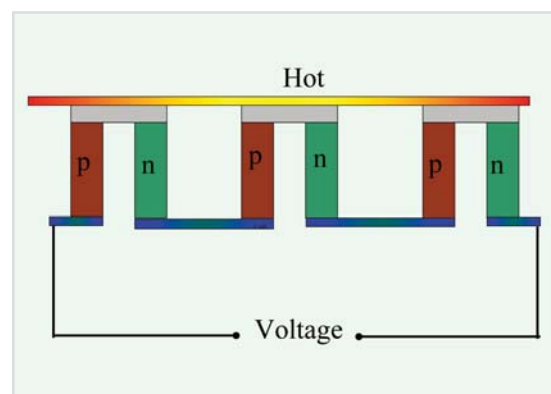


Fig. 1: Schematic presentation of a Thermo-electric Generator. It may be noted that thermo-electrical elements have electrical connection in serial mode and thermal connection in parallel mode.

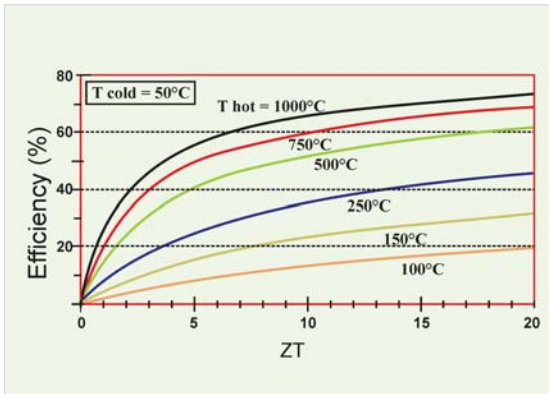


Fig. 2: Typical curves showing efficiency as a function of ZT of a thermoelectric material

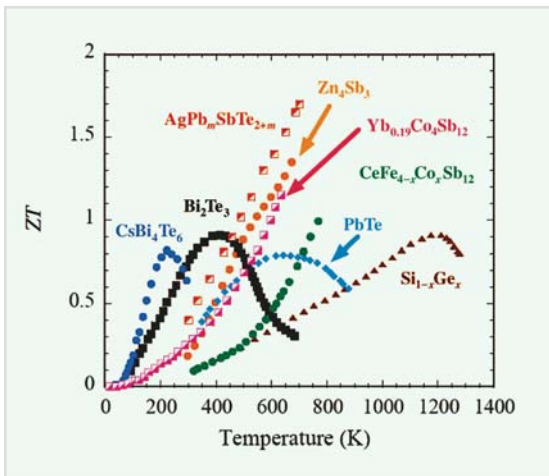


Fig. 3: ZT as a function of temperature for various thermo-electrical materials

rejected at the cold end of the device may be utilized as input heat for another device, giving rise to a ‘cascaded design’ for maximum heat utilization thus maximizing efficiency.

**FeSi<sub>2</sub> – based Thermoelectric Materials**

Semiconducting β-FeSi<sub>2</sub> is a promising material for high temperature thermoelectric applications due to its high resistance to oxidation, good thermo-power, relatively high electrical conductivity and non-toxicity. However, β-FeSi<sub>2</sub> is stable only up to 986° C, above which it decomposes into metallic α-Fe<sub>2</sub>Si<sub>5</sub> and ε-FeSi phases. The formation of the FeSi<sub>2</sub> phase occurs through a sluggish peritectoid

reaction α + ε → β because of which, synthesis of this phase involves prolong annealing treatments. Generally, the synthesis of FeSi<sub>2</sub> is done either by arc melting or by mechanical alloying elemental powders [10-12]. In this process, the resultant alloy does not contain sufficient amount of the β-phase and, therefore, long annealing treatments at lower temperatures are generally needed, to stabilize the desired volume fraction of the β-phase. For making an n-type and a p-type alloy, FeSi<sub>2</sub> is doped with Co and Mn, respectively.

In the present study, a different approach has been adopted. The FeSi<sub>2</sub> based alloys were firstly prepared by arc melting a mixture of high purity elemental constituents, in a water-cooled copper crucible, under inert argon gas atmosphere. The melting operation was repeated several times to achieve chemical homogeneity. The compositions of n-type and p-type alloys were kept at Fe<sub>0.94</sub>Co<sub>0.06</sub>Si<sub>2</sub> and Fe<sub>0.91</sub>Mn<sub>0.09</sub>Si<sub>2</sub>, respectively. This step ensured the required chemical homogeneity as well as the needed volume fractions of the parent phases.

The microstructures and the phases present in the as cast buttons, were examined by optical microscopy and X-Ray Diffraction (XRD) patterns. XRD of alloy buttons exhibited the presence of the α and the ε phases. Micrographs of polished cast specimens also showed a two-phase mixture (Fig.4). The gray phase, α - Fe<sub>2</sub>Si<sub>5</sub> was distributed throughout the matrix of ε-FeSi phase. At places, very fine particles of α were found to be segregated. Since arc melting involves melting and rapid cooling, the α + ε → β peritectoid reaction was suppressed resulting in a mixture of α and ε phases in the as-cast microstructure.

In the second step, the alloy buttons obtained by arc melting were crushed and ground to fine powders. These powders were subjected to consolidation in Vacuum Hot Press (VHP) at a temperature of 950 °C, 25 MPa pressure for 1 h. The vacuum hot pressed blocks were transformed

to  $\beta$ -FeSi<sub>2</sub>, which was subsequently confirmed by XRD. Present route, therefore, offered a clear cut advantage as it reduced a 20-100 h long annealing times of the conventional powder metallurgy processing, to transform the  $\beta$  - phase [13], into a short time of one hour. Fig. 5 shows 55 mm diameter blocks of alloys prepared by this new route.

The VHP blocks were cut into 4 x 4 x 10 mm specimens for the evaluation of Seebeck coefficient. For a typical specimen, Seebeck coefficient was found to be  $\sim 160 \mu\text{V/K}$  and an open circuit voltage of 90 mV was obtained through a single pin of 4 x 4 x 10 mm at a temperature difference of 750 K between the cold and hot ends (Figs.6-7). The VHP blocks of n-type and p-type alloys were cut into 'legs' and

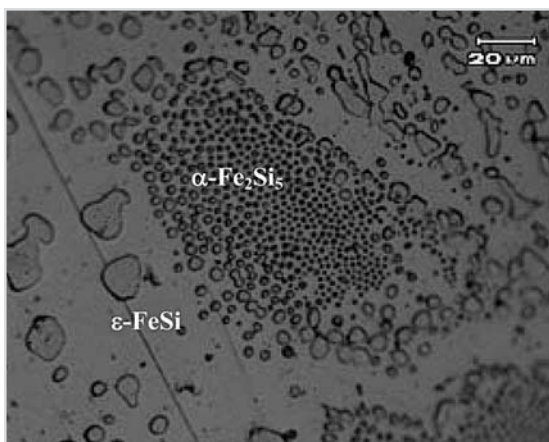


Fig. 4: As cast microstructure of FeSi<sub>2</sub> showing the presence of  $\epsilon$ -FeSi and  $\alpha$ -Fe<sub>2</sub>Si<sub>5</sub> phases.



Fig. 5:  $\beta$ -FeSi<sub>2</sub> blocks prepared by the new route

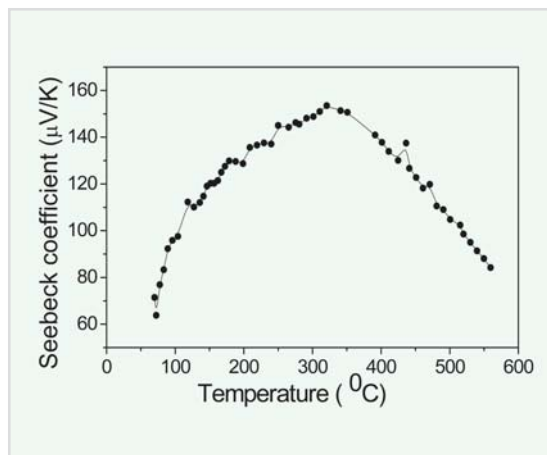


Fig. 6: Seebeck Coefficient of  $\beta$ -FeSi<sub>2</sub>

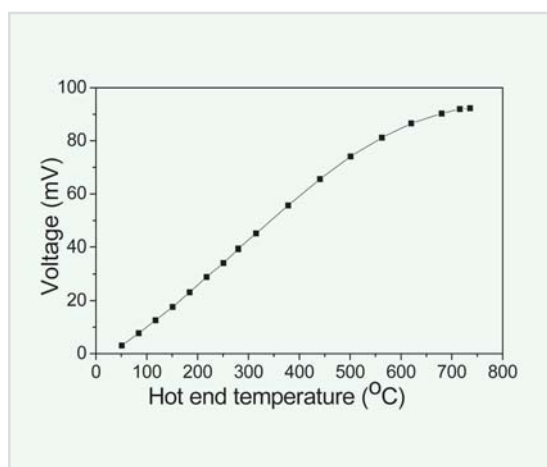


Fig. 7: Open Circuit voltage from a FeSi<sub>2</sub> leg

joined in 'Pi' type elements in a thermal insulating housing, for fabricating a miniature device (Figs.8-9). The n-p legs were electrically joined using platinum hardware and fritless silver paste. A characterization set up has been designed, to measure the power out put of device as shown in Fig.10. The power output from a 2-couple device was  $8 \mu\text{W}$  at the  $100^\circ\text{C}$  hot end temperature which increased sharply to 3 mW at  $600^\circ\text{C}$  (Fig.11).

### Oxide Thermoelectric Materials

Use of oxide thermoelectric materials for high temperature applications started in 1997, with the discovery of NaCo<sub>2</sub>O<sub>4</sub> [14]. Oxides are very attractive for such functional applications due to the potential





Fig. 8:  $\beta$ -FeSi<sub>2</sub> thermo-elements

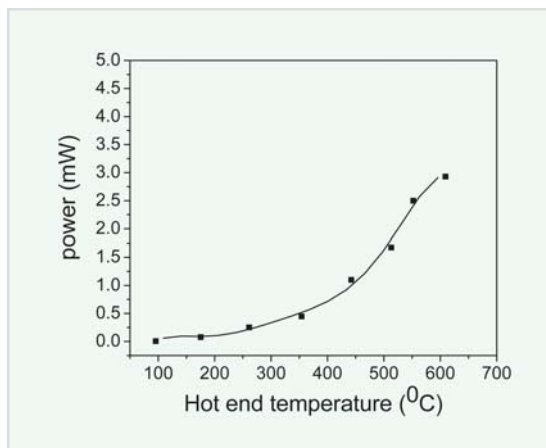


Fig. 11: Power output of FeSi<sub>2</sub> TE device properties

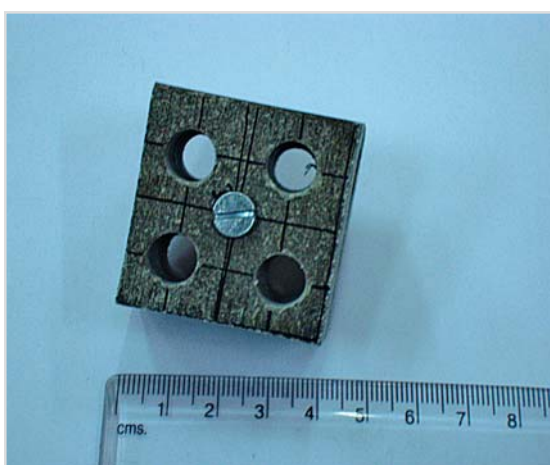
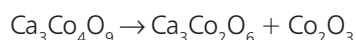


Fig. 9: Housing for thermoelectric device



Fig. 10: Measurement set-up for thermoelectric device

maneuverability of their properties with doping different cations. Till date, various oxide materials have been discovered for such applications e.g. Ca<sub>3</sub>Co<sub>4</sub>O<sub>9</sub>, BaPbO<sub>3</sub>, CaMnO<sub>3</sub>, NiO, ZnO etc. In the present work, results on Gd doped Ca<sub>3</sub>Co<sub>4</sub>O<sub>9</sub> (termed as 349-phase) and La doped CaMnO<sub>3</sub> are presented. Both these materials were synthesized in bulk by the controlled combustion synthesis route. In this processing route, thermal dehydration of aqueous solutions containing metal nitrates and a carbonaceous ‘fuel’ gives rise to a viscous gel which on further heating undergoes auto-combustion. Subsequent calcination of auto-combusted precursors may be required, to obtain desired oxide powders. Citric acid and manganese acetate have been used as fuel, for the synthesis of *p*-type Ca<sub>2.75</sub>Gd<sub>0.25</sub>Co<sub>4</sub>O<sub>9</sub> and *n*-type Ca<sub>0.92</sub>La<sub>0.08</sub>MnO<sub>3</sub>, respectively. Ultra-fine powders (average particle size < 1 μm) were obtained after calcination at 800 °C. These powders were subsequently consolidated. Ca<sub>0.92</sub>La<sub>0.08</sub>MnO<sub>3</sub> powders were compacted and sintered at 1250 °C in air to nearly full density (Fig.12). On the other hand, Ca<sub>2.75</sub>Gd<sub>0.25</sub>Co<sub>4</sub>O<sub>9</sub> powders could not be heated to temperatures higher than 950 °C, because the 349-phase is known to decompose into 326-phase according to the following reaction:



Therefore,  $\text{Ca}_{2.75}\text{Gd}_{0.25}\text{Co}_4\text{O}_9$  (CGCO) powders were vacuum hot pressed at  $900^\circ\text{C}$  to nearly dense pellets (Fig.13).

The dense compacts of *n*-type as well as *p*-type ceramics were cut into pins of dimensions 4 mm x 3 mm x 8 mm for measurement of properties and subsequent integration into miniature devices. The fabricated *n*-type pin of  $\text{Ca}_{0.92}\text{La}_{0.08}\text{MnO}_3$  (CLMO) has shown the Seebeck coefficient and electrical conductivity of about  $110\ \mu\text{VK}^{-1}$  and  $100\ \text{Scm}^{-1}$

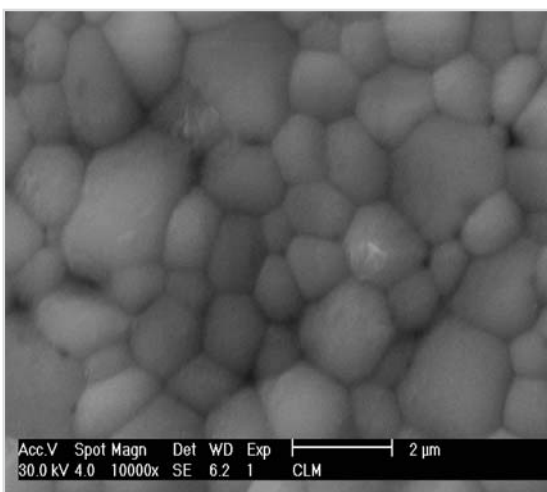


Fig. 12: Micrograph of  $\text{Ca}_{0.92}\text{La}_{0.08}\text{MnO}_3$  sintered at  $1250^\circ\text{C}$  in air

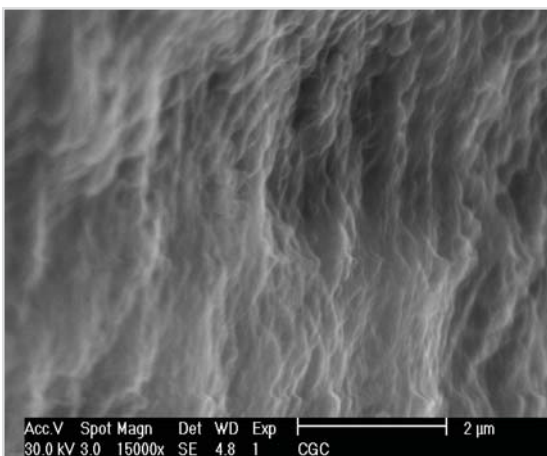


Fig. 13: Fracture surface of  $\text{Ca}_{2.75}\text{Gd}_{0.25}\text{Co}_4\text{O}_9$  vacuum hot pressed at  $900^\circ\text{C}$

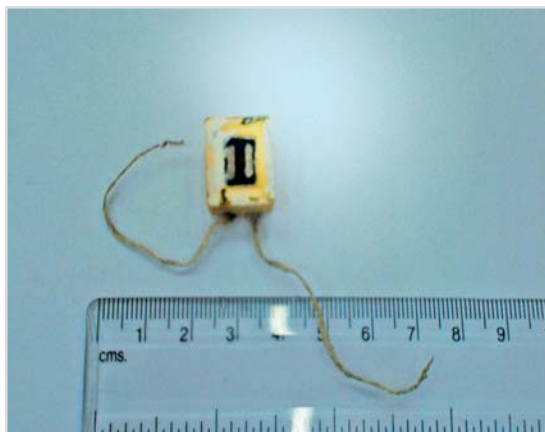


Fig. 14: Miniature oxide thermoelectric device

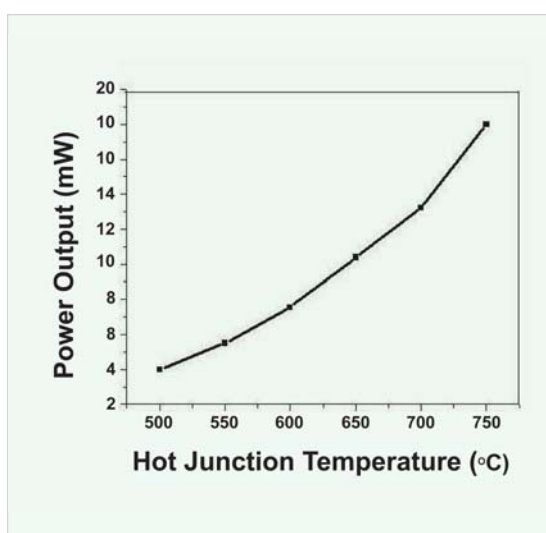


Fig. 15: Power output of oxide TE device

whereas the *p*-type pin of  $\text{Ca}_{2.75}\text{Gd}_{0.25}\text{Co}_4\text{O}_9$  exhibited the Seebeck coefficient and electrical conductivity of  $140\ \mu\text{VK}^{-1}$  and about  $85\ \text{Scm}^{-1}$  at  $800^\circ\text{C}$ , respectively. These functional properties obtained for both the ceramics indicated their suitability for high temperature thermo-electric devices. For making electrical contacts, each leg was coated with Pt-paste and subsequently these legs were electrically joined by a platinum mesh. A two-couple device was integrated using the above *n*-type and *p*-type pins as shown in Fig.14. The device showed a power output of 18 mW at the hot end temperature of  $750^\circ\text{C}$  (Fig.15).

## Development of electrical contacts with improved electrical, mechanical and thermal properties

For high temperature applications, contact material has to be metallurgically bonded to get significant lower contact resistance [15,16]. Silver based materials (including its alloys and composites) and platinum are the most popular contact materials for the oxide based high temperature thermoelectric devices.

A silver based composite, which is stable in air up to about 930 °C, has been used, for the development of efficient electrical contact. Tapes of the contact material with typical thickness of 50-100 μm have been prepared, using organic-based slurry through the Doctor-blade tape casting technique. These tapes were placed over faces of thermo-electric powder columns and were hot pressed along with thermo-electric materials using a multi-cavity die. The quality of metallurgical bonding of the hot-pressed thermo-elements, was tested for the adherence test, which showed that the bond strength of the contact was higher than 6 MPa. Such a high strength is indicative of a good quality metallurgical bonding of the contact with thermo-elements. The hot-pressed thermo-elements with the silver-based metallization were subjected to resistivity measurements as a function of temperature. The contact produced by the present technique showed, that in the temperature range 700-800°C, the resistance contribution of the contact was about 17-18% of the total internal resistance, against the conventional value of 40-50%. Therefore, the process has been further taken up for the fabrication of multi-elements for multi-component devices. Fig. 17 shows a photograph of hot-pressed multi-elements with contacts.

### Related issues for performance enhancement

Performance of a thermoelectric device can be improved by two ways: by increasing the figure of

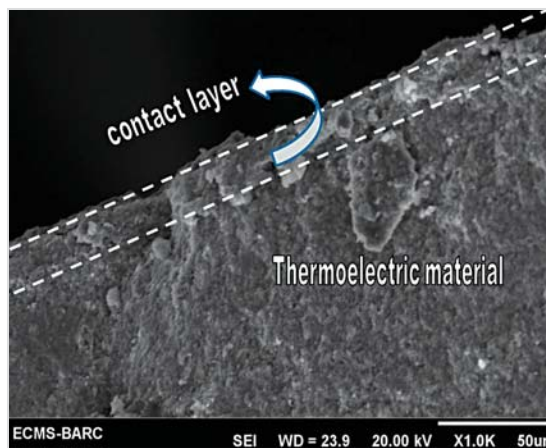


Fig. 16: SEM micrograph showing metallurgically bonded thermoelectric material with the contact material developed using hot press technique.

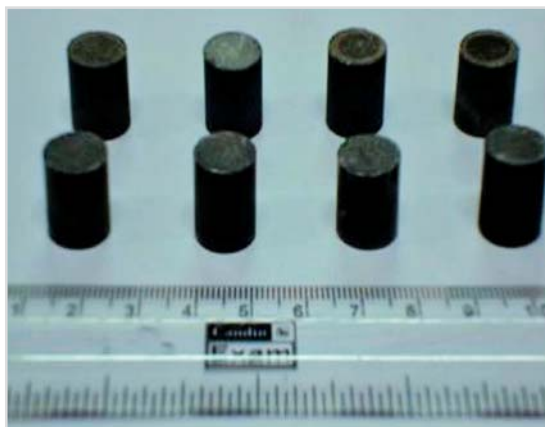


Fig. 17: Photograph showing hot pressed thermo-elements with contacts

merit  $Z$ , which calls for improving material properties like electrical conductivity, thermal conductivity and Seebeck coefficient, and/or by increasing the packaging density of the device.

Thermoelectric properties of  $\text{FeSi}_2$  based materials may be further enhanced, by dispersing fine oxide particles in the matrix. Initial experiments on this study have given encouraging results. Another relevant area of the study is the transformation of any residual  $\alpha$  or  $\epsilon$  phases in the VHP blocks into  $\beta$  phase using post-VHP annealing treatment.

In the case of oxide TE ceramics, doping of rare-earth elements are expected to change the functional

properties. It is, therefore, interesting to change the stoichiometry of TE oxides systemically and study its effect on the transformation temperature as each rare-earth element has its own specific charge ratio, thus stabilizing the 349 phase. Further work is being continued, for making multi-elemental devices for higher power output. The research work on the development of better electrical contacts with improved thermal and electrical characteristics for lowering parasitic resistances and increased power, is of utmost importance. In this context, a novel conceptual design of *monolithic* multi-element device has been proposed, and a dummy device using surrogate material has been fabricated.

### Summary

Thermoelectric materials based on intermetallic FeSi<sub>2</sub> as well as oxide ceramics were developed for high temperature applications. For β-FeSi<sub>2</sub> based alloys, such as n-type Fe<sub>0.94</sub>Co<sub>0.06</sub>Si<sub>2</sub> and p-type Fe<sub>0.91</sub>Mn<sub>0.09</sub>Si<sub>2</sub>, a new synthesis route involving a combination of arc-melting and VHP produced the material of same quality within hour against conventional time of production of 100 hours. The elements were cut from the VHP blocks of the synthesized material and a two-couple miniature device was fabricated. The device exhibited 3 mW power at 600 °C. The oxide ceramic materials n-type Ca<sub>0.92</sub>La<sub>0.08</sub>MnO<sub>3</sub> and p-type Ca<sub>2.75</sub>Gd<sub>0.25</sub>Co<sub>4</sub>O<sub>9</sub> were synthesized by combustion technique. These were consolidated into dense pellets by air sintering and VHP, respectively. A miniature device has been fabricated from the elements cut from consolidated pellets. The device showed power output of 18 mW at 750 °C. In addition, improvised electrical contacts were prepared using silver composite which lowered the internal resistance of the device to one third of the conventional values.

### Acknowledgements

Authors are thankful to Dr. K. Bhanumurthy, Head, SIRD, Dr. Madangopal Krishnan, Head, Functional Materials Section, MSD, Dr. G. K. Dey, Head, MSD

and Dr. S. C. Gupta, Head, TPD for fruitful suggestions and for providing facilities. We are grateful to Dr. A. K. Suri, Director, Materials Group for his keen interest, constant encouragement and support.

### References

1. K.H.J. Buschow, R. W. Cahn, M.C. Flemmings, B. Ilshner, E.J. Kramer, S. Mahajan (eds.), *Encyclopedia of Materials Science and Technology*, vol. 10, Elsevier, (2001).
2. D.M. Rowe (ed.), *CRC Handbook of Thermoelectrics*, CRC press, London, (1995).
3. K. Nogi, T. Kita, X.-Q. Yan, *Mater. Sci. & Engg.*, A307, 129-133, (2001).
4. M. Kubo, M. Shinoda, T. Furuhashi, K. Kitagawa, *Energy*, 30, 2156-2170, (2005).
5. Deep Prakash, M. Syambabu, C. Gayner, R. Tewari and P.K. Sinha, *PM-11, International Conference on Powder Metallurgy*, February 3-5, Pune, India (2011).
6. W. Shin, N. Murayama, K. Ikeda and S. Sago, *Jpn. J. Appl. Phys., Part 1*, 39, 1254, (2000).
7. I. Matsubara, R. Funahashi, T. Takeuchi, S. Sodeoka, T. Shimizu and K. Ueno, *Appl. Phys. Lett.*, 78, 3627, (2001).
8. Oxide TE – J. G. Noudem, S. Lemonnier, M. Pravel, E. S. Reddy, E. Guilmeau and C. Goupil, *Key Engg. Mater.*, 352, 245-250, (2007).
9. G. H. Rinehart, *Prog. Nucl. Energy*, 39, 305-319, (2001).
10. H. Nagai, K.-I. Nagai, T. Katsura, S. Katsuyama, K. Majima and M. Ito, *Mater. Trans. JIM*, 39, 1140-45, (1998).

11. A. Sugiyama, K. Kobayashi, A. Matsumoto, K. Ozaki and T. Nishio, *J. Jap. Inst. Met.*, 63, 1145-48, (1999).
12. W.-S. Cho and K. Park, *J. Mater. Sci: Mater. Elec.*, 11, 319-24, (2000).
13. W.-S. Cho, S.-W. Choi and K. Park, *Mater. Sci. & Engg.*, B68, 116-22, (1999).
14. I. Terasaki, Y. Sasago and K. Uchinokura : *Phys. Rev. B* 56, R12685, (1997).
15. T. Caillat, J.-P. Fleurial, G. J. Snyder, A. Zoltan, D. Zoltan, and A. Borshchevsky, A New High Efficiency Segmented Thermoelectric Unicouple, 34<sup>th</sup> Intersociety Energy Conversion Engineering Conference p. 2567 (1999).
16. R. Funahashi, S. Urata, K. Mizuno, T. Kouuchi and M. Mikami, *Appl. Phys. Lett.* 85 1036 (2004).

## Forthcoming Meeting

### DAE – BRNS Theme Meeting on Emerging Trends in Applications of Lasers & Accelerators in Nanomaterials (ETALAN-2011)

ETALAN-2011 will be held on 20 – 21 October, 2011, at the Multipurpose Hall, Training School Hostel, BARC, Anushaktinagar, Mumbai. It is being organized by the Radiation & Photochemistry Division, BARC and the Indian Society for Radiation and Photochemical Sciences (ISRAPS).

The theme meeting aims at discussing the current status and future challenges in the following areas:

- Synthesis & Characterization of nanomaterials using lasers & accelerators
- Modification/tuning of properties of nanomaterials using lasers & accelerators
- Fast & Ultra fast Spectroscopy on and with nanomaterials using lasers & accelerators
- Use of nanomaterials in lasers & accelerators.

Scientific sessions will include invited talks by experts as well as young researchers across the country and poster presentations of contributory papers.

All correspondence should be addressed to:

#### Secretary, ETALAN-2011

Radiation & Photochemistry Division  
Bhabha Atomic Research Centre,  
Trombay, Mumbai 400 085  
E mail: etalan2011@gmail.com  
Tel: 91-22-25590297, 25590309  
FAX: 91-22-25505331

# Development and Fabrication of Superconducting Hybrid Cable-In-Conduit-Conductor (CICC) for Indigenous Fusion Programme

A.K. Singh, M.M. Hussain, K.K. Abdulla and R.P. Singh  
Atomic Fuels Division

## Abstract

The Atomic Fuels Division has initiated development and fabrication of CICC of various configurations, for superconducting fusion grade magnets required for our indigenous Fusion Programme. The process involves development of high grade superconducting multifilamentary wire, multi stage cabling of superconducting as well as copper wires and, finally, jacketing of the cables in SS316LN tubes. The overview of the development and fabrication of CICC is presented in this article.

## Introduction

Thermo-nuclear fusion plasmas are magnetically confined in devices known as Tokamaks. The magnetic confinement is attained by steady or time varying magnetic fields, produced by large high current carrying superconducting magnets. These robust superconducting magnets are usually constructed of cables of NbTi, Nb<sub>3</sub>Sn & Nb<sub>3</sub>Al superconductor composites incorporated within cable-in-conduit-conductor (CICC) configurations. The most important requirement is that the superconducting CICC be stable in the operating reactor plasma environment. CICC constitutes more than one sixth of the cost of a fusion reactor.

The Institute for Plasma Research and the Atomic Fuels Division, BARC have launched a joint initiative towards an indigenous development of fusion grade superconductors and cables. This effort is ultimately aimed at generating a complete technology and process know-how, for making fusion grade superconductors and cables and using these for developing prototype of large size, high field, high current carrying magnets.

## Fabrication Technology

The fabrication technology of superconducting CICC consists of the following stages:

- a) Superconducting wire fabrication
- b) Cabling and wrapping
- c) Insertion and Jacketing.

### a) *Superconducting wire fabrication*

The most critical component of a CICC is the multifilamentary superconducting wire, that is capable of carrying very high currents required for the generation of intense magnetic fields. Niobium-Titanium and Nb<sub>3</sub>Sn superconducting composites have quite a long history in the era of applied superconductivity. Virtually, all of the large superconducting magnet systems that have been constructed so far, have used Nb-Ti or Nb<sub>3</sub>Sn superconductors. The Nb-Ti alloys are ductile and can be co-processed with copper into a wide range of composite conductors. On the other hand, Nb<sub>3</sub>Sn is a brittle inter-metallic compound and is created by heat treatments carried out at the end of the

fabrication cycle. While the Nb<sub>3</sub>Sn based CICC is used for high field application (~12 Tesla), the Nb-Ti based CICC is only suitable for low field application. The fabrication of Nb-Ti based fusion grade CICC is discussed in this paper.

The parameters important in the design of a superconductor are [1]:

- a) Critical temperature  $T_c$ .
- b) Critical magnetic field  $H_c$ .
- c) Critical current density  $J_c$ .

Both  $T_c$  &  $H_c$  are dependent only on the chemical composition of the alloy, whereas the critical current density  $J_c$ , is a structure dependent property and is strongly affected by the density, size and distribution of imperfections such as, dislocations, grain boundaries and precipitates, which can act as flux pinning centers [3].

The fabrication parameters are crucial to achieving a suitable microstructure in the composite conductors and the required electrical and mechanical properties. The underlying composite material fabrication technology needs to be fine-tuned to meet a range of disparate demands such as, adequate mechanical strength or the right combination of superconducting and normal conducting properties, for obtaining stabilization.

The steps involved in the fabrication of superconducting wire are:

1. Preparation of hexagonal elements
2. Assembly of these elements in OFHC copper sleeve to form extrusion billet
3. EB welding of the billet assembly
4. Hot Extrusion
5. Cold drawing with intermediate vacuum ageing treatment and
6. Twisting.

Based on an extensive development work carried out, which included composite billet design, optimisation of parameters for extrusion, drawing and ageing treatment to obtain suitable shape, size

and distribution of  $\alpha$ -Ti precipitates for flux pinning centres, an appropriate fabrication route has been standardised for 0.80 mm dia. wire containing ~500 Nb-Ti filaments, each of 25 micron size, with Cu:SC (matrix to superconducting element) ratio of 1.15:1. Single length wires of 10 Km have been successfully produced [3,4], which show a maximum critical current of 1500 Amps (measured in short samples in 5.5 Tesla field and 4.2 K). Fig. 1 shows the typical cross section a 0.80mm dia SC wire. Fig. 2 shows

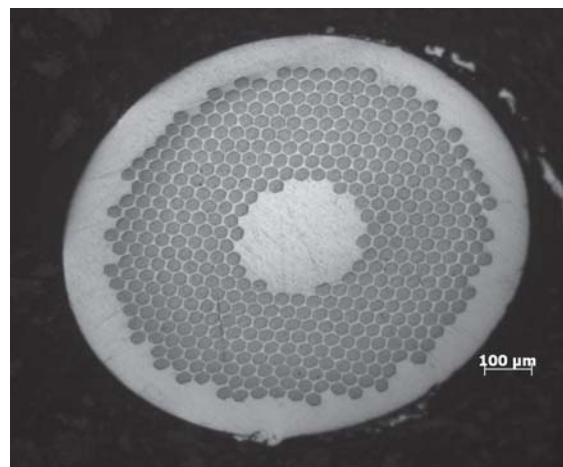


Fig. 1: Cross-section of 0.8 mm strand showing Nb-Ti filaments

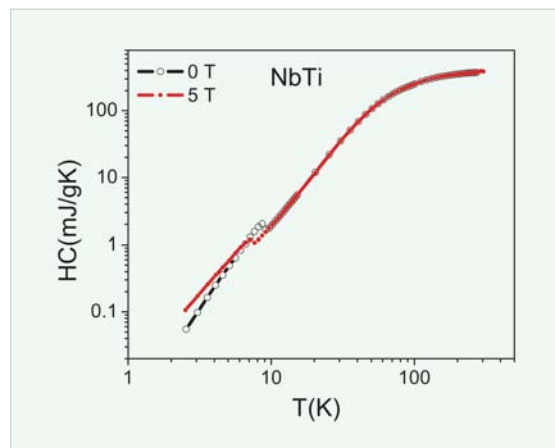


Fig. 2: The second order normal to superconducting phase transition under 0 T and 5 T fields

the normal to superconducting second order phase transformation at ~9.8K, while Fig. 3 shows the

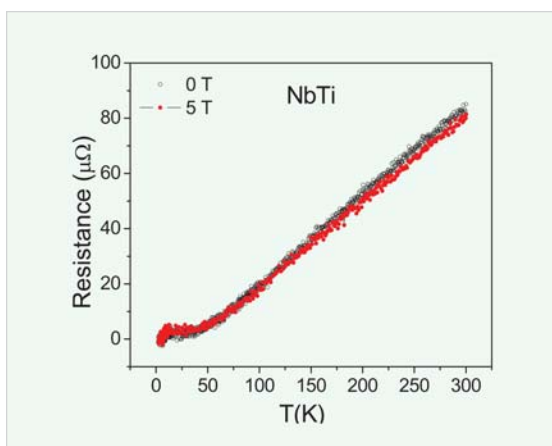


Fig. 3: Resistance Drop with temperature under 0 T and 5 T fields

resistance drop with temperature in absence and presence of a 5 Tesla field (these results are for a 0.80mm dia wire).

### b) Cabling Technology

The problem of stability is an important criterion for the design of all practical superconducting wire magnets [2]. On account of the resistance in the normal state being very high and also the current density employed in these magnets being high, a local transition from superconducting to normal state causes intense local heating. With the heat spreading to neighbouring regions of the winding, the normal zone spreads rapidly till a point, when all stored energy is dissipated as heat. Compared to other types of superconducting magnets, the superconducting wire ones are susceptible to this 'degradation' or 'quenching' phenomenon at much lower currents. However, degradation is ameliorated by making a composite conductor in which the superconductor wire is in intimate contact with a good thermal conductor such as OFHC copper: local cooling is provided to each conductor in winding. Additionally, the cabling is designed to provide sufficient voids for flow of super fluid Helium through the CICC.

The cabling of a CICC involves several stages of twisting that are dictated by the physical application

and the engineering aspects. These details were first thoroughly investigated and followed by several hardware trials with available infrastructure and machineries to develop an optimized design of the CICC. The schematic of the optimized twisting pattern is shown in Fig.4. The cable obtained after stage 4 is shown in Fig.5.

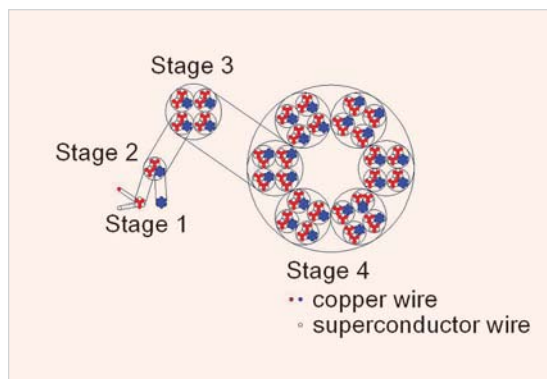


Fig. 4: Schematic of the multi stage cabling pattern



Fig. 5: Final Stage Cable Containing 504 wires of 0.8 mm dia

### c) Jacketing Technology

We have developed an indigenous swaging method for jacketing the cable. Here, the final stage cable is wrapped in a half-overlap pattern with SS304L tape and inserted into a round SS316LN tube of suitable size. This is further compacted and shaped into a square cross section by swaging. The finished CICC is wound onto a 2m dia. barrel spool using a bender.



Figs. 6 and 7 show the duplex swaging machine utilised for jacketing and the square cross section swaging die, respectively. The pulling force is a critical parameter in this method and determines the void fraction of the CICC. This technique has specific advantages over the conventional technique in which the jacketing is done by longitudinal seam welding of a strip cold rolled onto the cabled conductor [2].

The latter technique requires careful automated welding to avoid heating of the cabled strands (the conventional technique has been used in the CICC of Steady State Tokamak (SST) -1 coming up at IPR, Gandhinagar).

A 60m long 30kA hybrid CICC of 30mm x30mm square cross section has been fabricated by the



Fig. 6: Duplex Swaging machine at AFD, BARC



Fig. 8: Foil wrapping on final stage cable



Fig. 9: Insertion of wrapped cable in circular tube

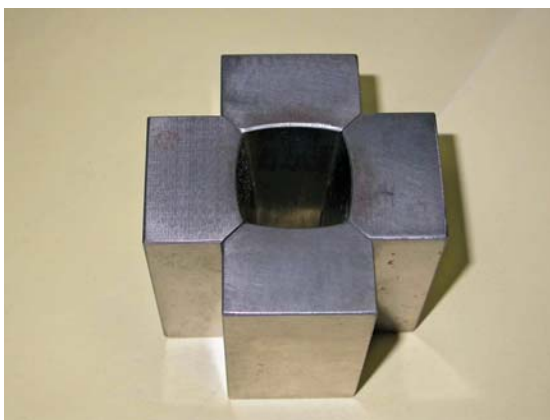


Fig. 7: Swaging Die developed at AFD, BARC



Fig. 10: Swaging of SS316LN tube containing cable to Square cross section CICC



Fig. 11: Bending of CICC



Fig. 12: CICC in 2m dia coil form

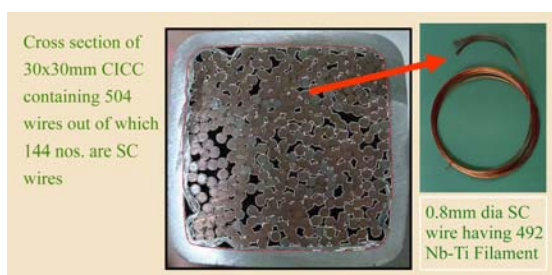


Fig. 13: Cross section of CICC

indigenous technique. Figs. 8 -13 show some of the important stages of fabrication.

The CICC developed at BARC has shown a current carrying capacity of 11000 A at 6 K, against the designed value of 10000 A at 4.5 K supercritical helium. Apart from this, the hybrid conductor has about 25% less superconductor compared to that used in SST-I.

## Future Work

An on-line fabrication facility is being set up using several shop floor innovations that will facilitate the fabrication of CICC in a comparatively smaller space. The facility consists of foil wrapping setup, a triangular mechanised cable insertion system, orbital welding machine along with tube handling system, a set of swaging, bending and coil winding machines. Several trials have already been carried out for the insertion of final stage wrapped cable made of copper wire in SS tube, the orbital welding of these tubes containing cable, the round to round as well as round to square swaging and bending with coil winding. Further optimisation of the process is in progress.

## References

1. P. J. Lee and D. C. Larbalestier, "Development of nanometer scale structures in composites of Nb-Ti and their effect on the superconducting critical current density" *Acta Metall.*, Vol. 35 (No. 10), 1987, p 2523-2536.
2. F. Hosono, G. Iwaki, S. Inaba, T. Suzuku, K. Hiroshima, K. Kikuchi, K. Chida, M. Watahiki, K. Kamata, Subrata Pradhan and Y. C. Saxena, "Production of Nb-Ti CICC's for SST-1 project at IPR" *IEEE Trans. On Applied Superconductivity*, Vol. 11, No. 1, March 2001 p 2014-2017.
3. A. K. Singh, M. M. Hussain, S. P. Singh and V. G. Date, "Low Temperature Superconductor – Fabrication and Application." ATM, IIM, Vadodara, Nov. 14-17, 2002 & News Letter, IIM Mumbai Chapter, p 12-18, Dec., 2002.
4. A. K. Singh, M. M. Hussain, S. P. Singh and R. P. Singh "Fabrication of multifilamentary Nb-Ti superconducting wire and cable: technological capabilities available at Atomic Fuels Division, BARC" *BARC Newsletter*, May 2004, No. 244, p 11-14.

# Multi-Detector Environmental Radiation Monitor with Multichannel Data Communication for Indian Environmental Radiation Monitoring Network (IERMON)

M.D. Patel, M.P. Ratheesh, M.S. Prakasha, S.S. Salunkhe,  
A. Vinod Kumar, V.D. Puranik and C.K.G. Nair (Retd.)  
Environmental Assessment Division

## Abstract

A solar powered system for online monitoring of environmental radiation with multiple detectors has been designed, developed and produced. Multiple GM tube detectors have been used to extend the range of measurement from 50 nano Gy/hr to 20 Gy/hr and to enhance the reliability of the system. Online data communication using GSM based and direct LAN based communication has been incorporated. Options for use of power supply from mains powered and battery powered have been enabled. Care has been taken to make it weather-proof, compact, elegant and reliable. The development is a part of the ongoing program of country-wide deployment of radiation monitors under "Indian Environmental Radiation Monitoring Network (IERMON).

## Introduction

Fears about nuclear radiation and its effects are often raised in the media and in the general public. The success of establishment of large scale nuclear power programme envisaged by our country, also depends on the public perception about nuclear radiation. Adequate number of online and realtime radiation monitoring systems along with availability of the information in the public domain, will inform the public about the omnipresent environmental radiation due to natural sources and its geographical variation. Display of marginal or insignificant change in the radiation levels due to establishment of nuclear power plant as compared to natural background radiation will eliminate the false propaganda of increase in radiation levels in the public domain. In addition, a countrywide network of environmental radiation monitor serves as an early warning system for detection and for activating emergency response in case of an unlikely event of

nuclear emergency either in our own country or in the neighbouring countries.

Ionizing radiation has always been a part of the human environment due to cosmic rays and due to the natural radioactive elements present in the earth's crust. The natural radiation is of: a) Terrestrial origin b) Cosmic origin. The terrestrial radiation is due to the presence of naturally occurring radioactive substances like Uranium, Thorium and Potassium isotope (K-40) in earth's crust. Cosmic radiation comes through the earth's atmosphere, from the sun and galaxies. This increases with latitude & altitude. It is more at poles than at equator.

It is essential that a system which is meant for detection of nuclear emergency must be installed in open environment so that the changes in environmental radiation level can be readily and accurately monitored. The traditional systems work on mains power which is subject to various problems

like load shedding, power fluctuations, power transients etc. Also it is inconvenient to provide mains power when the system is required to be installed in the field in remote areas. It is found that provision of battery backup is not sufficient in the cases involving extended or frequent power shutdown. Hence, it is desirable that the environmental monitor is powered by other sources of power such as solar panels, wind turbines, etc. with battery backup.

Data communication is another requirement for effective monitoring. The radiation incident should be reported with minimum possible time lag. Hence, the system should have redundant communication channel. Presently the technologies available for data communication from field systems are (1) land line telephone (dialup and leased line), (2) mobile phone network (GSM and CDMA), (3) VSAT, (4) RF, etc.

Indian Environmental Radiation Monitoring Network (IERMON) is a countrywide network of online monitoring stations located at various parts of the country and with central monitoring station located in Mumbai. The network is designed, developed, established and managed by the Environmental Assessment Division of Bhabha Atomic Research Centre, Mumbai. The network employs systems developed indigenously, keeping in mind the general and strategic requirements of the country, also geographical condition and available resources for power and communication.

### The new IERMON System

The new IERMON system employs multiple radiation detectors for redundancy and extended range of measurement. The system has multichannel data communication facility. The system works on solar power with battery backup. It is designed with the following capabilities:

- **Zero Down Time:** The system is ensured to work reliably at any point of time. Adequate redundancy has been provided in measurement

and data communication. All components are of MIL grade, wherever possible.

- **Low Maintenance:** The requirement of visiting the site for preventive maintenance and/or calibration check is not more than once in an year.
- **Easy Maintenance:** It is easy for a trained layman to carry out the maintenance.
- **Outdoor Installation:** The system is designed for outdoor installation for measurement of natural background radiation as well as enhanced radiation levels due to accidental release of radioactivity into the atmosphere.
- **Energy Harvesting:** The system uses a natural power source like solar power pack for its working.
- **Ease of Communication:** Low cost and easy availability are the main criteria for selecting mode of data communication. The system in addition, has wired communication for local display and redundancy.
- **Weather proof:** The system operates at ambient air temperature between  $-20^{\circ}\text{C}$  and  $+60^{\circ}\text{C}$  and ambient relative humidity up to 100%.

The technical specification of the system developed are :

### 1. Environmental and Fallout Dose Measurements

Detected radiation	: Gamma radiation
Detectors	: Energy compensated GM tubes
Energy response (combined)	: 35 keV to 2 MeV
Measurement range (combined)	: 50 nanoGy/h to 20 Gy/h

(Gy = Gray, keV = kilo electron Volt, MeV = Mega electron Volt)

### 2. Environmental

Operating temperature	: $-20^{\circ}\text{C}$ to $+60^{\circ}\text{C}$
Relative humidity	: up to 100%

System enclosure : IP68 compliance for detectors & Electronics Housing.  
IP66 for battery housing with support for solar panel.

EMI/EMC : IEC applicable standards.

The high voltage (HV) required for GM1 and GM2 is 450V and for GM3 it is 550V. Separate HV module is implemented for GM1 and GM2, though both the tubes can be operated from a single supply. Using separate HV module enhances redundancy but it leads to increased power consumption. Selection of HV module is critical for this reason.

**3. Power Supply**

- Solar panel, 20W, 9V
- Sealed Maintenance Free Battery, 6V/24Ah

**4. System Description**

The following types of radiation detectors are used in the system:

- High sensitivity GM counters (GM1 and GM2 in Fig. 1)
- Low sensitivity GM counter (GM3 in Fig. 1)

To reduce the power consumption only one way transmission i.e. from system to central station is activated, though the system is capable of two way communication. The LAN Socket Modem shown in the block diagram (Fig. 1) is for LAN based communication. Fiber-based communication and satellite-based data communication can be added with little modification, if such facility is available at local station. This port is also used by service engineer for interfacing with computer at the time of system maintenance/calibration.

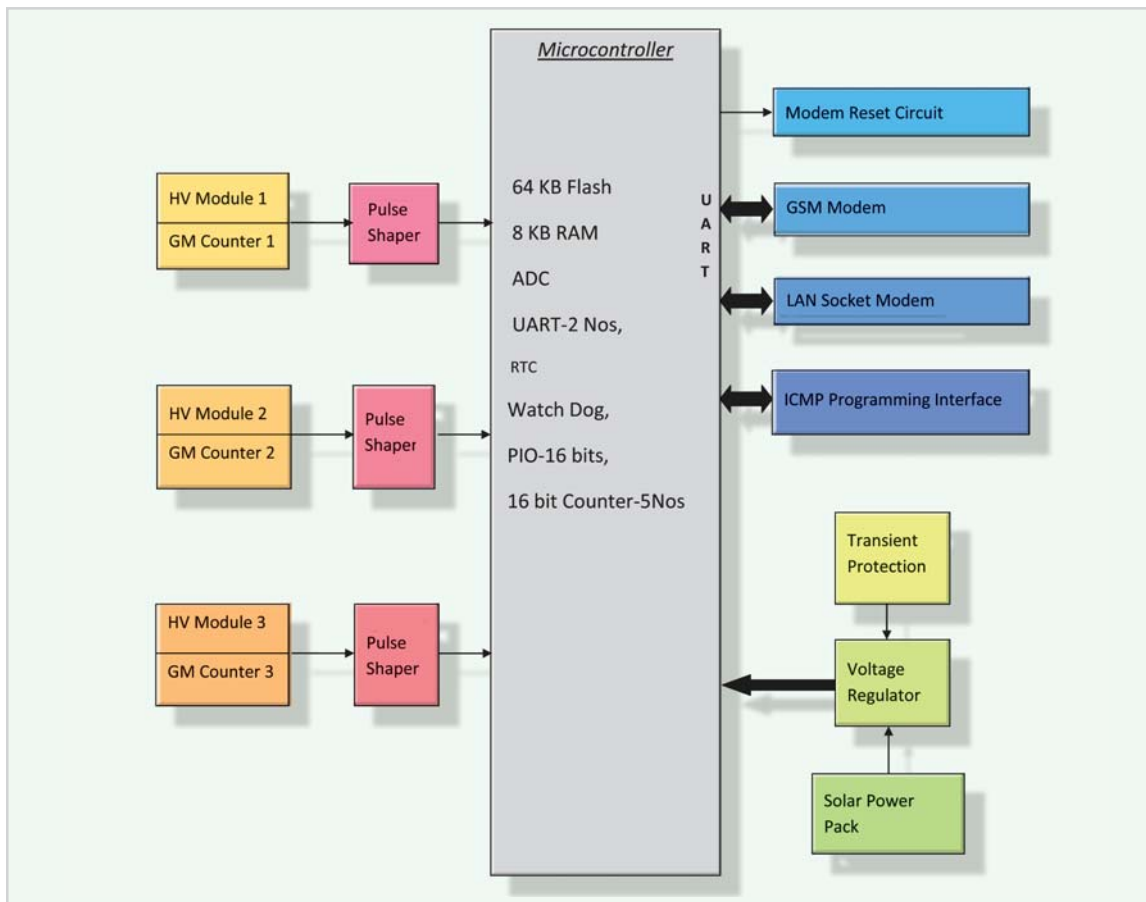


Fig. 1: Block diagram of the IERMON system

The Solar Power Pack consists of solar panel, charge control relay and SMF (Sealed Maintenance Free) battery. The present system is designed to operate using 20W solar panel with 6V/24Ah battery. The system can work for 15 days in a cloudy weather condition using only the supply from the back up battery. Transient Suppression Devices are used to protect the system from electrical transients that may enter the system through the cable from solar panel.

The pulses from the GM counters are converted to transistor transistor logic (TTL) pulses using Pulse Shaper circuits. The TTL pulses from the Pulse Shaper are fed to the inputs of the counters of the micro controller.

The micro controller is programmed to read the counter values at every five minutes without disturbing the counter. The extrapolated hourly dose is computed from the counts and checked with the preset trigger level for verifying any abnormal increase of radiation. If at least two out of the three detectors agree on exceeding a certain trigger level, an 'event flag' is set and the processor transmits the dose level every five minutes until the dose level falls below the trigger level. Normal averaging time is one hour and is synchronized with the Real Time Clock (RTC). At the end of the counting

period (signalled by the 'end-of-hour' interrupt from RTC), the counts are converted to dose rate using appropriate conversion factor derived from the calibration lookup table. Necessary correction is applied if the counting time is less than one hour, as normally the case when the system is started or restarted. The hourly dose is stored in memory. A photograph of the printed circuit board (PCB) of the system and the complete system is shown in Fig. 2 and Fig. 3.

The system performance has been tested in the field for about 6 months. The system has performed uninterrupted, unattended as per the technical requirement in the field conditions.

### Applications of the new IERMON System

The new IERMON System was designed for deployment in the countrywide Indian Environmental Radiation Monitoring Network (IERMON). More than 100 such systems have been deployed all over India and it is targeted to achieve installation of 500 units in a span of 2 years. The system can also be used for other applications involving measurement of environmental gamma radiation. In cases where operation using mains power is required, the system can accommodate an SMPS board. The system can also be used only with built-in battery and with this, the system can work for six months in data logging mode without communication. For in-plant monitoring, where the system is powered by mains, power data communication can be also achieved through the existing telephone lines.

### Acknowledgements

The authors are indebted to Director, Health Safety & Environment Group and Associate Director, Health Safety & Environment Group, BARC for their constant support and inspiration. This work would not have been successful without the active participation of the members of the divisional workshop and other colleagues in the Environmental Systems and Networking Section of the division.



Fig. 2

Fig. 3

Fig.2 PCB showing detector locations in IERMON System (PCB Size : 8.5cm x 45cm)

Fig.3 Photograph of complete IERMON System (Height : 90cm; Base Plate : 30cm x 30cm ; Weight : 25kg)

# Mapping Interfaces in Magnetic Thin Films with Neutron Reflectometry

Saibal Basu and Surendra Singh

Solid State Physics Division

## Abstract

The article discusses the importance of Polarized Neutron Reflectometry (PNR) in understanding magnetic structure of thin films. A PNR has been installed in the guide tube laboratory of Dhruva reactor. This instrument has been used successfully, to understand magnetic structure in thin films. Some of the results obtained on magnetic non-magnetic multilayer samples have been presented, to demonstrate how PNR has been successful in characterizing interface magnetic structure.

## Introduction

Polarized neutron reflectometry is one of the most important non-destructive tools, in understanding and characterizing interfaces in various thin films of interest. Historically Fermi and Zinn were the first to report in the pages of *Physical Review* journal in 1946, neutron reflectivity measurement for finding out coherent nuclear scattering cross-section of various materials [1]. Approximately a decade later the first report on x-ray reflectivity for thin film characterization from L. G. Parratt appeared [2]. The reincarnation of neutron reflectometry as a useful tool for studying thin films and interface magnetic structure is due to G. P. Felcher of Argonne National Laboratory in 1980s. Later, his comments in a popular article written in *Neutron News* is worth mentioning [3]:

*“Ten years ago at a modest spallation-neutron source at Argonne National Laboratory, a “gizmo” was installed which was later christened as a reflectometer. The popularity of the gizmo spread like wild fire: now virtually all neutron sources possess at least one of them. Some are graced by splendid names: CRISP and SURF at Rutherford, TOREMA at Jülich, DESIR in Saclay and EVA in Grenoble.”*

It is the rich information content with resolution in nanometer length scale regarding physical and magnetic structures of thin films, that has made Polarized Neutron Reflectometry (PNR) such an important and popular tool. The popularity of neutron reflectometry is well augmented by that of X-ray Reflectometry (XRR). Both use the phenomena of reflection of waves from thin film surfaces. Since the x-rays interact with the atomic electron cloud and the neutrons with the nuclei, the refractive index for x-rays depends on the electron density of the material and the refractive index for neutrons depend on the coherent scattering length density for neutron-nuclear interaction in the material. This basic difference makes them complementary techniques for study of surfaces and interfaces in thin films. In addition, the neutron possesses a magnetic moment of  $-1.91 \mu_N$  (nuclear magneton) and PNR is ideally suited for understanding magnetic structure of multilayer samples. PNR has gained importance also because of rapidly growing interest in thin film multilayers of magnetic and non-magnetic materials, giving rise to various important effects like Giant Magneto-Resistance and Spin-Valve effects. These are artificial

materials that are important, fundamentally as well as technologically. Spin Valve based DRAM memory devices have already appeared in the market. It is important to characterize these materials at nanometer length scale, to correlate their property-structure relationship. In recent years PNR has come handy in such studies. Another important property of neutrons is its capability to distinguish between the isotopes: hydrogen and deuterium, because the coherent scattering lengths are quite different for these two isotopes. This makes neutron an ideal tool to study liquid air or liquid/liquid interfaces and organic films. Presently neutron reflectometry technique is considered so important, that the Rutherford Appleton Laboratory, U. K. in their recently installed second target station at ISIS spallation neutron source, has installed a so-called neutron reflectometer "village" consisting of three neutron reflectometers: one designed for horizontal sample geometry targeting liquid-air interfaces, one for vertical sample geometry for studying magnetic interfaces and another one for studying off-specular or diffuse reflectivity from surfaces and interfaces.

A Polarized Neutron Reflectometer (PNR) has been built in the Dhruva guide tube laboratory by the Solid State Physics Division, BARC. This reflectometer is being used routinely to study magnetic structure in multilayer and thin films. We will briefly discuss some of the results obtained from this instrument on samples of interest.

**Brief Exposition to Neutron Reflectometry**

A neutron at grazing incidence, experiences an average potential in a medium, arising from neutron–nucleus interaction:

$$V(R) = \frac{2\pi h^2}{m} \rho(R) b_{coh} \tag{1}$$

Where 'V(R)' is the number density of the scattering centres in the medium and 'b<sub>coh</sub>(R)' is the coherent scattering length for each scattering centre. This

potential translates to a refractive index 'n' for a medium, given by

$$n = 1 - \frac{\lambda^2}{2\pi} \rho b_{coh} \tag{2}$$

Where λ is the wavelength of the neutron, This simple expression tells us that depending on the sign of 'b<sub>coh</sub>', the refractive index can be less than or more than 1. For most materials 'b<sub>coh</sub>' is positive and the refractive index is marginally less than 1: n = 1 - δ, where δ is typically about 10<sup>-5</sup>-10<sup>-6</sup>. Neutrons are totally reflected up to a critical incident angle θ<sub>c</sub>' given by:

$$\theta_c = \lambda \sqrt{\frac{\rho b_{coh}}{\pi}} \tag{3}$$

For a good reflector like nickel, the value of wavelength dependent critical angle θ<sub>c</sub> is 6 arc minutes / Å. For a medium in which the scattering centres have magnetic moments, neutrons, because of their inherent magnetic moment, will experience a potential energy in a field 'B(R)', other than the nuclear potential, given by:

$$V_{mag}(R) = -\overline{\mu N \cdot B}(R) \tag{4}$$

If one considers that the film is so magnetized that the magnetic moments are all aligned giving the internal field 'B(R)', then the refractive index of the medium for polarized neutrons is given by:

$$V(R) = \frac{2\pi h^2}{m} \rho(R) [b_{coh} \pm b_{mag}] \tag{5}$$

We have defined a magnetic scattering length 'b<sub>mag</sub>' arising out of 'V<sub>mag</sub>', where, the sign before the magnetic scattering length depends on the neutron magnetic moment parallel (+) or anti-parallel (-) with respect to the polarization of the sample. We will use the term up (+) and down (-) for these two polarizations. Also, now the critical angles for total external reflection for up (+) and down (-) neutrons are different:



$$\theta_c^\pm = \lambda \sqrt{\frac{\rho[[b]_{coh} \pm b_{mag}]}{\pi}} \tag{6}$$

This shows that polarized neutron reflectometry from magnetic samples will enable one to map the magnetic field in a magnetic sample. Above the critical angle, once the neutron beam starts penetrating the medium, it gets reflected at every interface due to refractive index contrast and the reflected amplitudes interfere. The measured reflectivity becomes structured. The oscillations in reflectivity profile above the critical angle bear the signature of layered structure of a thin film.

Fig. 1 shows simulated PNR profiles ( $R^+$  and  $R^-$ ) for a Fe-Cr multilayer thin film for up (+) and down (-) neutrons. The reflectivity profile has been plotted as a function of momentum transfer ' $Q$ '  $\vec{Q} = \vec{K}_i - \vec{K}_f = \frac{4\pi}{\lambda} \sin\theta_i$  for specular reflection]. The scattering geometry has been shown in Fig. 2. In specular reflectivity, angle of incidence ( $\theta_i$ ) and angle of reflection ( $\theta_r$ ) are equal. We will show

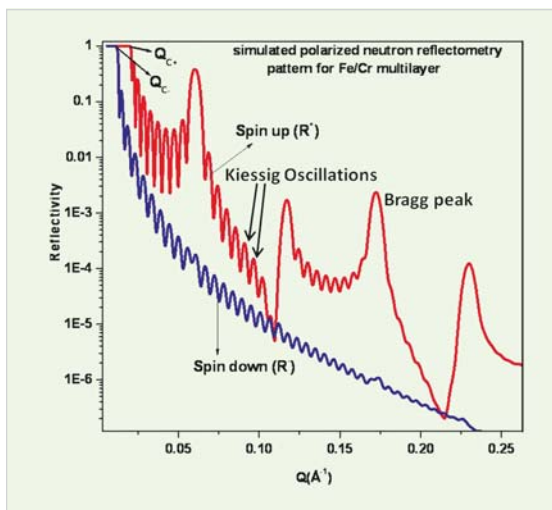


Fig. 1: Spin-up ( $R^+$ , red line) and spin-down ( $R^-$ , blue line) reflectivity profile for an Fe/Cr multilayer thin film consisting of 10 bilayers of Fe and Cr. The Bragg peaks are due to periodicity of the bilayers and the Kiessig oscillations are signature of total thickness of the film. The critical angle for  $R^-$  is lower than  $R^+$  because refractive index for '+' and '-' neutrons are different

data plotted either as functions of ' $Q$ ' the momentum transfer or as functions of angle of incidence.

The Fe-Cr film consists of ten periodic bilayers of Fe-Cr with each bilayer approximately 10 nanometer (nm) thick: total thickness being 100 nm. The

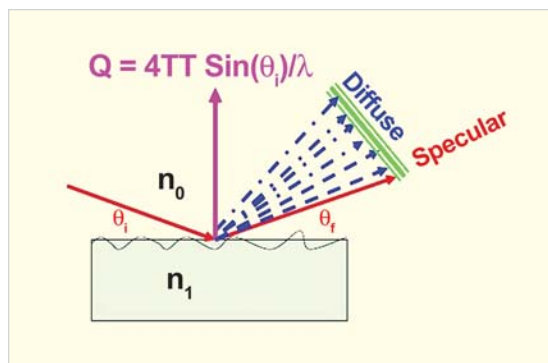


Fig. 2: The scattering geometry for neutron reflectometry. For specular reflectivity, angle of incidence ( $\theta_i$ ) equals angle of reflection ( $\theta_r$ ) by Snell's law. For off-specular reflectivity this equality does not hold (blue rays). Roughness at the interface gives rise to off-specular reflectivity.

difference in the critical angles between ' $R^+$ ' and ' $R^-$ ' is due to the difference in potential seen by '+' and '-' neutrons. The periodic repetition of the bilayer gives rise to so-called "Bragg peaks" in the reflected intensity, similar to the diffraction peaks arising from atomic periodicity in crystal lattices. The oscillations in intensity between two Bragg peaks are due to the interference of neutron waves, reflected from the top and bottom the film. These are called "Kiessig oscillations" and are signatures of total thickness of the film. The Bragg peaks are absent in  $R^-$  due to the fact, that for the down neutrons there is a loss of contrast between Fe and Cr layers [negative sign in potential, eqn. (5)] and the periodic structure of the film is lost. This example brings home the point, that the profiles  $R^+$  and  $R^-$  bear the signatures of physical and magnetic structure of the Fe-Cr thin film.

## Polarized Neutron Reflectometer in Dhruva

The PNR instrument in Dhruva had been installed on a curved neutron guide in Dhruva. Neutron guide tubes transport neutrons using the phenomenon of total external reflection from guide walls. The present guide tubes at Dhruva, glass coated with Ni, were fabricated and installed by the Solid State Physics Division, to take neutron beams out from the reactor hall to guide tube laboratory. Fig. 3(A) shows a photograph of the reflectometer and schematic of the same is shown in Fig. 3 (B) [4]. The reflectometer has been designed for vertical sample geometry and it can be used for specular as well as off-specular (or diffuse) reflectometry (when angle of incidence is not equal to angle of reflection). The neutron beam coming from Dhruva reactor through the curved guide is reflected by [113] planes of a Si monochromator, to select a monochromatic beam of 2.5 Å neutrons [neutron beams shown by red

arrows in Fig. 3 (A)]. These neutrons are collimated to few arc minutes using a collimator made from Cd slits. The collimated and monochromatic beam of neutrons can be polarized using a polarizing super mirror made from Co-Fe/Ti-Zr layers. This monochromatic, highly-collimated and polarized beam of neutrons is reflected from a vertical sample, magnetized using a permanent magnet of 2K Gauss strength and located at the centre of a rotation stage. With the sample fixed at the centre, the sample stage is rotated in steps (typically about 1 arc minute) to collect the reflectivity pattern of the sample as a function of angle of incidence ( $\theta_i$ ). Fig. 3 shows the scattering geometry. In specular reflectivity, angle of incidence ( $\theta_i$ ) and angle of reflection ( $\theta_r$ ) are equal. Since we use a PSD in this instrument, we have the liberty to collect off-specular reflectivity data also on this instrument [ $\theta_i \neq \theta_r$ ]. Off-specular reflectivity can reveal surface and interface morphology. Presently we will discuss results of specular reflectometry only.

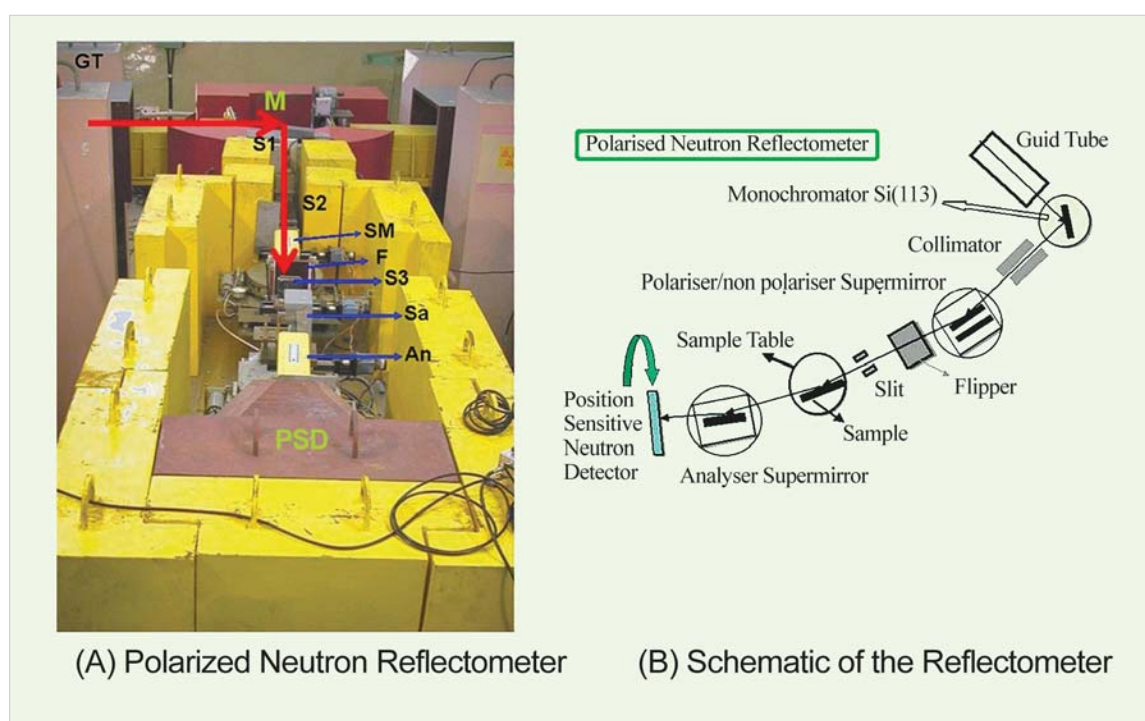


Fig. 3: (A) Photograph of the polarized neutron reflectometer at Dhruva and (B) schematic of the same. 'M' is the monochromator, 'S1 S2 S3' are the cadmium slits for collimator, 'SM' is the super mirror polarizer, 'Sa' is the sample stage with magnet, 'An' is the analyzer super mirror and 'PSD' is the  $^3\text{He}$  position sensitive neutron detector.

The rotation stage can rotate with a precision of about 20 arc seconds and is capable of carrying a load up to 400 Kg. It had been designed and fabricated in the Centre for Design and Manufacture, BARC specifically for the reflectometer. The reflected beam is detected by a 30 cm long  ${}^3\text{He}$  neutron Position Sensitive Detector (PSD), fabricated in the solid state physics division. The PSD has a position resolution of approximately 2 mm. The D. C. flipper in the beam is used to flip the direction of neutron spins for measuring reflectivity for spin-up (+) and spin-down (-) neutrons. Due to intensity constraints we do not use a spin analyzer for the reflected beam at present, though the analyzer is available. In the present set up, we are able to determine physical and magnetic moment density as a function of depth in the sample.

Some of the results are discussed here to demonstrate the importance of polarized neutron reflectometry in pinning interface structure of thin films.

### Data Collection and Analysis

A stepper motor-based control system has been designed for the high precision translation and rotation stages. The monochromator is mounted on a tilt and rotation stage assembly. The spectrometer table can rotate around the monochromator to facilitate  $\theta - 2\theta$  coupling between the monochromator and the table. This allows changing the incident wavelength, if required. The collimator is mounted on a high precision linear stage, which can move the collimator in steps of 10 microns across the beam. The sample and the magnet are mounted on a linear stage with one-micron step size on top of the rotation stage. Sample surface is brought to the centre of the rotation stage with the help of this linear stage. The control system for all the stepper motors is an integral unit with the drivers and the power supplies located in it. It is operated from the instrument's PC through RS232 serial port communication.

Typical reflectivity data collected at a certain angle of incidence  $\theta_i$  looks like a Gaussian on the  ${}^3\text{He}$  PSD channels [insets, Fig. 4]. The integrated counts under the peaks, after background subtraction, give intensity at particular angles as shown in Fig. 4.

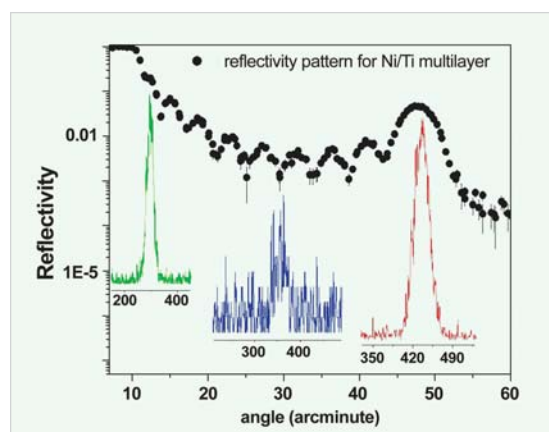


Fig. 4: A typical neutron reflectivity profile as a function of angle, collected on the PNR at Dhruva. The insets show intensity as a function of channel no. for a specific angle of incidence. Integrated intensity under each peak after background subtraction gives one data point in the reflectivity profile

The analysis of PNR data requires getting the structure of thin film sample in terms of layer thickness, magnetic moment density, interface composition and interface roughness from the experimental data in ' $Q$ ' space. Ideally, it is through a Fourier inversion from momentum space (' $Q$ ') one can get the structure (magnetic or physical) in real space (' $R$ '). In reality we can collect data only over a limited momentum ' $Q$ ' or angular range and direct Fourier transformation is not possible. We take recourse to a '*model-fitting*' where we start with an assumed structure of the thin film sample and generate a reflectivity pattern corresponding to this structure. The initial model is modified through a  $\chi^2$  minimization program, using some error minimization software to modify the physical parameters, so that we generate an intensity profile matching the experimental data. We have developed an optimization software using '*Genetic Algorithm*'.

## Samples Studied

### a. Ni/Ti multilayer

Thin film multilayers of Ni/Ti have found useful applications in the field of soft x-ray and neutron optics, where they are used as highly reflecting mirrors, supermirrors, polarizers and monochromators etc. Further, TiNi alloy prepared in thin film form, shows interesting shape memory effect and this has been utilized to develop different Micro-Electro Mechanical Systems (MEMS) such as cantilevers, actuators etc. Bulk Ni/Ti alloys are also important technological materials. We had prepared Ni/Ti multilayers of various modulation lengths on glass substrate by vacuum deposition. The sample discussed here had ten Ni/Ti bilayers [Ni 5 nm and Ti 7 nm] on glass substrate. The aim of the study was to understand the growth of alloys at the interfaces as a function of annealing [5]. The samples were annealed first at 300 °C and then at 400 °C for a fixed time of 1.5 h. PNR was carried out on all the samples before and after annealing. Fig. 5 shows the PNR data from the sample before and after annealing. The solid red circles are data for  $R^+$  and the open blue circles are for  $R^-$ . Solid lines are fits to the data. The drop in the intensity of the Bragg peak and the gradual merging of the profiles for  $R^+$  and  $R^-$  are due to mixing of Ni and Ti at the interfaces. We had also carried out XRR on the same sample (data not shown). Analyzing the XRR and PNR data, we derived the physical and magnetic structure of the sample. To highlight the complementary role of XRR and PNR, we show the plots of physical density as obtained from XRR from the sample before and after annealing at 300 °C and 400 °C together with the corresponding magnetic moment density profiles in Figs. 6 (i) and 6 (ii) respectively. The physical density of the as-deposited sample shows clear step-like oscillations of density as a function of depth [6(i) (a)] signifying periodic Ni and Ti layers of nearly bulk density. The corresponding magnetic moment density, obtained from PNR also shows the same step-like nature as a function of depth. Ni is the

magnetic component in this sample and we found an average magnetic moment of  $0.4 \mu_B$  (Bohr magneton) per Ni atom in the Ni layers and a zero magnetic moment density for the Ti layer from PNR data. As we annealed the sample, alloying occurred at the interfaces. Figs. 6(i)(b-c) clearly show progress of alloying at the interfaces as *snapshot* pictures of density profiles obtained from XRR. We determined the composition of the alloy layers at two interfaces, which showed small asymmetry for Ni on Ti with respect to Ti on Ni. This trend is also reflected in the magnetic moment density profile. The magnetic moment density profiles have been obtained from PNR data. As the alloying progressed at the interfaces, the magnetic layers got thinner as seen in Figs. 6(ii)(b-c). Only the Ni layers remained

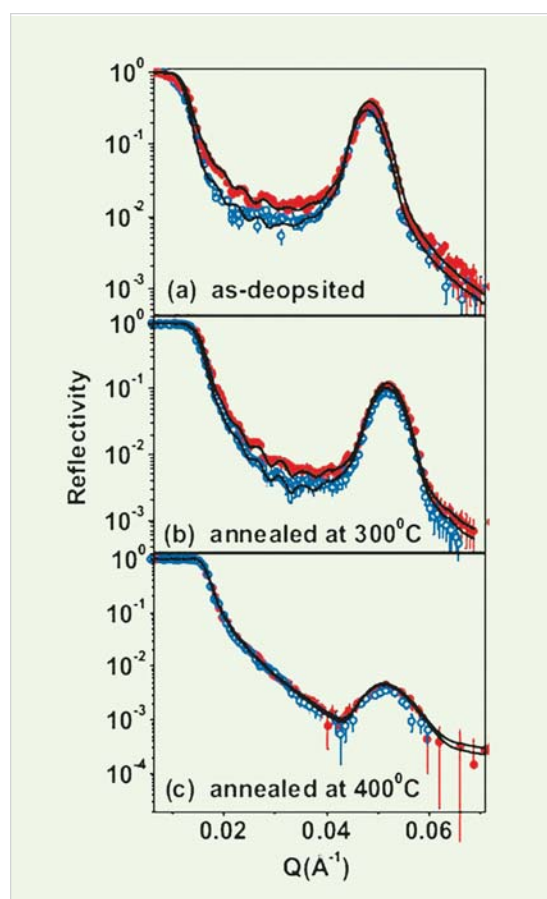


Fig. 5:  $R^+$  (red solid circles) and  $R^-$  (blue open circles) reflectivity profile from Ni/Ti multilayer sample along with the fits (black lines) for (a) as-deposited, (b) annealed at 300 °C and (c) annealed at 400 °C

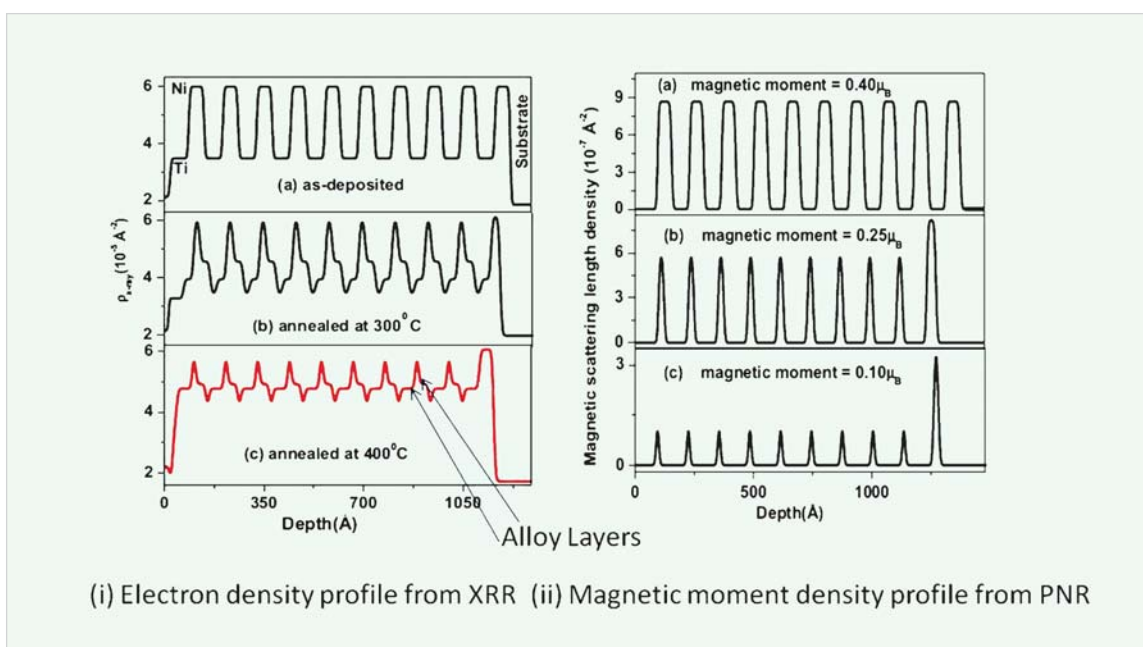


Fig. 6: (i) Electron density profile from XRR and (ii) Magnetic moment density profile from PNR for the Ni/Ti multilayer sample for as-deposited and annealed samples(a-c)

magnetic, the interface alloy layers and the Ti layers had zero magnetic moment density. Also the average magnetic moment per Ni atom reduced to  $0.1 \mu_B$  due to loss of neighbors for Ni atoms at the interfaces. This study allowed us to quantify the nature of alloying at Ni/Ti interfaces in this sample, physically and magnetically, with a spatial resolution of few nanometers! Such resolution is barely possible with any other technique.

### Fe-Au multilayers

A number of studies have been done in recent years in ferromagnetic/non-magnetic multilayer thin films with an aim to find the effect of interface structure on magneto-resistance. We have carried out a series of studies on Fe-Au multilayer samples [6]. We varied the Fe layer thickness systematically and obtained the interface structure in each case through PNR and XRR. Our aim was to correlate the magneto-resistance in these samples, with their physical and magnetic structure at the interfaces. Presently we discuss only the PNR data at Dhruva and the details of magnetic moment at the interfaces.

We obtained PNR data from 3 samples of nominal structure: Si Substrate/[Fe( $t_{Fe}$  nm)/Au(5 nm)]<sub>10</sub>, with  $t_{Fe} = 3, 5$  and  $10$  nm, respectively, indicating that the Fe layer thickness varied from 3 nm to 10 nm in these samples. The PNR data from 3 multilayer samples consisting of 10 bilayers of Fe/Au, as described above are shown in Fig. 7, (i)-(iii). The thickness of the Fe layer in each bilayer has been 3 nm, 5 nm and 10 nm in the three samples. For each sample we collected data for spin up (red solid circles) and spin down (open blue circles). The solid lines are the fits to the data. The "Bragg peaks" and "Kiessig oscillations" are clear in the data.

We could 'map' the details of the magnetic moment density at the interfaces in these samples from fits to the PNR data. Magnetic Scattering Length Density (SLD) at the interfaces of Fe/Au layers for all three samples with varying Fe layer thickness as obtained from PNR are shown in Fig. 8. It shows two interfaces of an Au layer, Au on Fe (Au/Fe) and Fe on Au (Fe/Au). Vertical dashed lines are the imaginary ideal interfaces. The gradual change in magnetic moment density across interface indicates

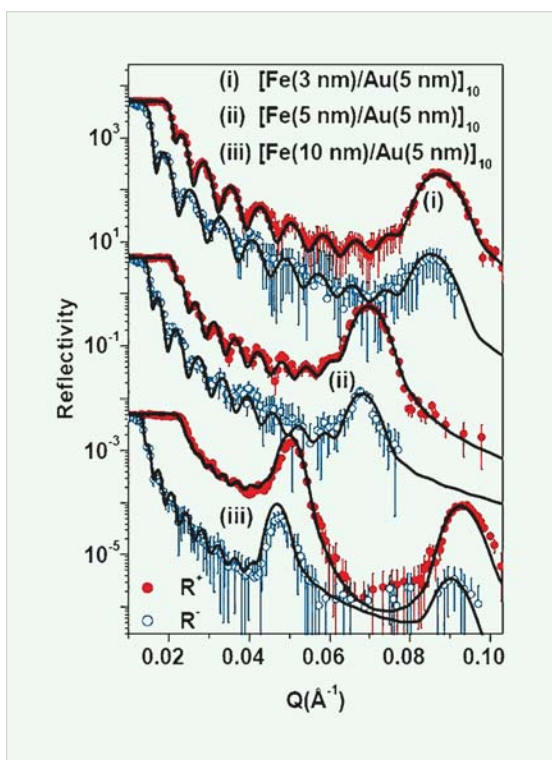


Fig. 7:  $R^+$  (red circles) and  $R^-$  (blue circles) for Fe/Au multilayers with varying Fe thickness from 3 nanometer to 10 nanometer (a-c) with Au layer thickness fixed at 3 nanometer. Solid lines are fits to the data

alloying between Fe and Au at the interfaces. The magnetic SLD reaches an average value in the Fe layer and becomes zero in the Au layer. It is also clear that there is a marked asymmetry in the magnetic SLD profile between Fe on Au and Au on Fe interfaces. This happened due to the difference in inter-diffusion of the two species Fe and Au during sputtering. Also for thicker Fe layer the SLD is higher. For Fe layer of 10 nm thickness, the magnetic moment corresponds to  $2.18 \mu_B$  (Bohr magneton) per Fe atom, close to the value known for bulk iron ( $2.2 \mu_B$ ). The multilayer with 10 nm thick Fe layer also showed larger change in magneto-resistance with respect to magnetic field compared to other samples. The present study shows that the magneto-resistance of a multilayer thin film is intimately related to its microscopic structure at the interfaces.

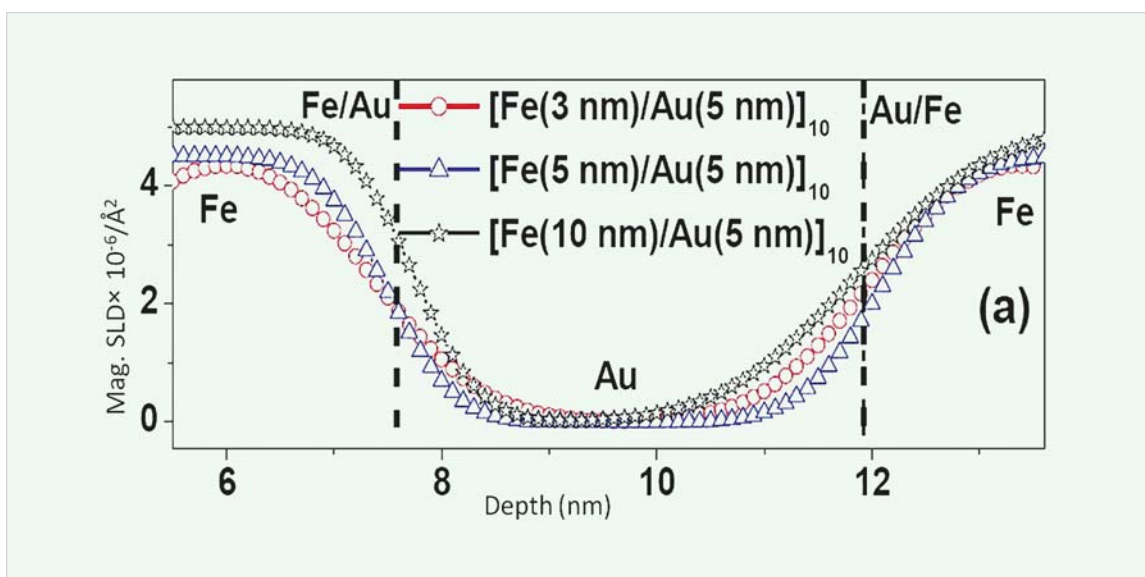


Fig. 8: Magnetic scattering length density (SLD) profile at the two interfaces of an Au layer in Fe/Au multilayer, from the fits to PNR data. The two interfaces are Fe on Au (Fe/Au) and Au on Fe (Au/Fe). The vertical dashed lines are imaginary, ideal interfaces

## Conclusions

We have discussed the importance of neutron reflectometry in understanding interface structures in magnetic multilayer thin films. A PNR has been designed and installed in Dhruva reactor guide hall, for characterizing such samples of interest. From data collected on this reflectometer on Ni/Ti and Fe/Au multilayers, we have shown how detailed characterization of interface structure is possible with nanometer resolution. These examples demonstrate that PNR as a characterization tool is extremely important for development of thin film based magnetic devices.

## Acknowledgements

The high precision rotation stage for the above reflectometer was designed and fabricated at the Centre for Design and Manufacture, BARC. The data collection software was developed at the Electronics Division, BARC.

## References

1. E. Fermi and W. Zinn, *Phys. Rev.*, 70, 103 (1946).
2. L. G. Parratt, *Phys. Rev.*, 95, 359 (1954).
3. G. P. Felcher, *Neutron News*, 5 (4) (1994).
4. S. Basu and S. Singh, *Journal of Neutron Research*, 14, 109 (2006).
5. S. Singh, S. Basu, P. Bhatt, and A. K. Poswal, *Phys. Rev. B* 79, 195435 (2009).
6. S. Singh, S. Basu, C. L. Prajapat, M Gupta and D. Bhattacharya *Solid State Physics* (India) 2010, to appear.

## India and CERN: Visions for Future Collaboration

A two-day meeting between scientists/engineers from India and CERN was held in the Multipurpose Hall of Training School Hostel, BARC, on 28<sup>th</sup> February and 1<sup>st</sup> March 2011. The meeting was organized on the advice of Chairman, AEC and Director General, CERN. The delegation from CERN was led by the Director General, R. Heuer. The meeting was to discuss future collaborations between CERN and India, in order to discuss the expanding role of India at CERN and the reciprocal benefits of CERN's scientific and technological base for Indian science and engineering. It covered the following topics : The CERN accelerator complex; Physics at the LHC; Highlights from non-LHC experiments, CLIC; Future detectors for particle physics; Medical applications of accelerators and detectors; Capacity building at CERN; Grid

computing & Education. A large number of delegates representing national institutes, universities and industries across the country, participated in the meeting.



Director General of CERN, R. Heuer, addressing the gathering



Dr. Srikumar Banerjee, Chairman, AEC with Director General of CERN



## Report on the seminar “Nanotechnology and Its Applications”

The Maharashtra Academy of Sciences (M.A.S) Mumbai Chapter, in collaboration with BARC, organized a one-day Seminar on Nanotechnology on May 9, 2011 at the Multi-purpose Hall, BARC Training School Hostel & Guest House at Anushaktinagar, Mumbai. The seminar was funded by the DAE-BRNS. The speakers were from Indian Institute of Technology, Mumbai, and BARC. About 180 participants including scientists, teachers, students and Mumbai-based Fellows of the Academy attended the seminar.

Dr K.B. Sainis, Director, Biomedical Group, BARC and also the Vice President of M.A.S. welcomed the delegates. Dr. A.M. Bhagwat, Ex-BARC scientist and the President of the Mumbai Chapter gave a brief account of the activities of the MAS Mumbai Chapter. Dr J.P. Mittal former Director, Chemistry Group, BARC and M.N. Saha Distinguished Fellow was the Chief Guest and delivered an enlightening address on the role of national science academies, in creating awareness about science and developing scientific thinking. He said that though the subject Nanotechnology was really not new, the attributes of a vast number of materials and structures needed to be explored to see whether they could be harnessed for technological applications in industry as well as in human health.

The seminar was conducted in three scientific sessions. The invited talk in the first session was delivered by Prof. Jayesh Bellare of IIT, Mumbai on the applications of nanotechnology like novel surfactants in respiratory diseases, nanocomposites for dental use, anticancer agents etc. for healthcare. In the second session, Prof. D. Bahadur (IIT, Mumbai) gave an account of extensive studies on hyperthermia and triggered drug release for cancer treatments through magnetic hybrids and nanoparticles. The invited talk in the third session was by Prof A.Q. Contractor of (IIT, Mumbai) on conducting polymers and their use in biosensors and activators. Dr. S.K. Gupta, Head, Technical Physics Division, BARC, presented a comprehensive account of the use of nanostructured semiconductor oxides for detection of gases. Dr. V.K. Suri of BARC talked about micro-engineering and nano-engineering techniques and capabilities that have been developed in BARC. In the final talk, Dr. J.V. Yakhmi former Associate Director, Physics group, BARC gave a bird's eye view of nanoscience and nanotechnology covering various aspects of applications in biology and medicine and underlined the need to inspire young students to take up research in this area.

The seminar ended with concluding remarks by Dr. K.B. Sainis, Director, Biomedical Group, BARC.

## National Technology Day celebration at BARC : a report

The National Technology Day was celebrated at the Central Complex Auditorium in BARC on 11<sup>th</sup> May 2011, to highlight the advances that we have made, in the field of Science & Technology during the year.

The Chief Guest on the occasion was Dr. V.K. Saraswat, Scientific Adviser to Raksha Mantri, Director General & Secretary, Defence Research & Development Organization, New Delhi.

Dr. Srikumar Banerjee, Chairman, Atomic Energy Commission & Secretary, Department of Atomic Energy welcomed the audience. He introduced Dr. Saraswat as the 'missile man', who had developed the missile 'Prithvi'. He also said that DAE & DRDO collaboration should be strengthened further.

Dr. V.K. Saraswat gave an invited talk on "Innovation through Technology". He said that he was inspired by the Prime Minister who had said that, 'Economic Growth will be possible only through Innovation'.



Welcome address by Dr. Srikumar Banerjee, Chairman, Atomic Energy Commission & Secretary, Department of Atomic Energy

Every year, the Department of Atomic Energy felicitates Scientists & Engineers of its various units, who have made outstanding R&D contributions, by awarding them the Homi Bhabha Science & Technology Award. The eight distinguished awardees, who were given this award in 2010, delivered talks in the morning session, on their R&D

work. Mr. S. Chattopadhyay, Head, BOD, BARC, Dr. Dinesh Srivastava, MSD, BARC, Dr. P.K. Mohapatra, RCD, BARC, Dr. Sadhana Mohan, Head, HWD, Dr. B.K. Nayak, NPD, BARC, Mr. K. Ananthasivan, IGCAR, Dr. Subhashis Chattopadhyay, VECC & Mr. P. Srinivasan, RPG, BARC. The speakers used simple informal language and presented their work in a lucid manner. The entire programme was well received by prominent scientists & engineers from the Department of Atomic Energy.



Invited talk by Dr. V.K. Saraswat, Scientific Adviser to Raksha Mantri, Director General & Secretary, Defence Research & Development Organization, New Delhi.

## BARC Scientists Honoured

**Name of the Scientist** : **Dr. A. K. Tyagi**  
Chemistry Division  
Honour : Fellow, Royal Society of Chemistry (FRSC)  
Conferred by : Royal Society of Chemistry, UK

---

**Name of the Scientist** : **Dr. Dimple P. Dutta**  
Chemistry Division  
Honour : Member, National Academy of Sciences,  
India  
Conferred by : National Academy of Sciences, India

---

**Name of the Scientist** : **Dr. Vinita Grover Gupta**  
Chemistry Division  
Name of the Award : Young Scientist Award  
Conferred by : Indian Society for Chemists and Biologists

---

**Name of the Scientist** : **Dr. H.S. Misra**  
Molecular Biology Division  
Honour : Member, Guha Research Conference  
Honoured at : Annual Meeting of GRC-2010, held at  
Aurangabad, Dec.16-21, 2010

---



Cajuput Tree

Edited & Published by :  
Dr. K. Bhanumurthy,  
Head, Scientific Information Resource Division,  
Bhabha Atomic Research Centre, Trombay, Mumbai 400 085, India.  
Computer Graphics & Layout : N. Kanagaraj and B. S. Chavan, SIRD, BARC  
BARC Newsletter is also available at URL: <http://www.barc.gov.in>